https://doi.org/10.5194/wes-2023-38
Preprint. Discussion started: 4 May 2023

eawe european academy of wind energy
Open Access WIND ENERGY SCIENCE DISCUSSIONS

Annual Variability of Wake Impacts on Mid-Atlantic Offshore Wind Plant Deployments

David Rosencrans[1,2], Julie K. Lundquist[1,2,3], Mike Optis[2,4], Alex Rybchuk[2], Nicola Bodini[2], and Michael Rossol[2]

[1]Department of Atmospheric and Oceanic Sciences, University of Colorado, Boulder, 80303, USA
[2]National Renewable Energy Laboratory, Golden, 80401, USA
[3]Renewable and Sustainable Energy Institute, Boulder, 80303, USA
[4]Veer Renewables, Courtenay, V9N 9B4, Canada

Correspondence to: David Rosencrans (David.Rosencrans@Colorado.edu)

Abstract

The mid-Atlantic will experience rapid wind plant development due to its promising wind resource located near large population centers. Wind turbines and wind plants create wakes, or regions of reduced wind speed, that may negatively affect downwind turbines and plants. Long mid-Atlantic wakes are causing growing concern. We evaluate wake variability and annual energy production with the first year-long modeling assessment using the Weather Research and Forecasting Model, deploying 12-MW turbines across the domain at a density of 3.14 MW km^{-2}, matching the planned density of 3 MW km^{-2}. Using a series of simulations with no wind plants, one wind plant, and complete build-out of lease areas, we calculate wake effects and distinguish the effect of wakes generated internally within one plant from those generated externally between plants. The strongest wakes, propagating 58 km, occur in summertime stable stratification, just when New England's grid demand peaks in summer. The seasonal variability of wakes in this offshore region is much stronger than diurnal variability of wakes. Overall, the mean year-long wake impacts reduce power output by 35.9%. Internal wakes cause greater year-long power losses (27.4%) compared to external wakes (14.1%). Additional simulations quantify wake uncertainty by modifying the added amount of turbulent kinetic energy (TKE) from turbines, introducing power output variability of 3.8%. Finally, we compare annual energy production (AEP) to New England grid demand and find that the lease areas can supply roughly 60% of annual load.

1 Introduction

The U.S. offshore wind industry is flourishing, with a target capacity of 30 GW by 2030 (White House, 2021). New England features the highest population density in the United States and commensurate utility usage, making offshore wind an attractive regional electricity source. Twenty-seven active lease areas now span the mid-Atlantic Outer Continental Shelf (OCS). The

https://doi.org/10.5194/wes-2023-38
Preprint. Discussion started: 4 May 2023

eawe european academy of wind energy
Open Access WIND ENERGY SCIENCE DISCUSSIONS

OCS features low turbulence (Bodini et al., 2019) and fast winds, with 100-m winds averaging 10 m s^{-1} (Musial et al., 2016). Consequently, large wind plants will be constructed to harness the ample wind resource.

Meteorological conditions and construction challenges constrain siting options for large wind plants. Because the average wind direction is southwesterly (Bodini et al., 2019), a southwest-to-northeast wind plant orientation mitigates external waking from neighboring plants. Further, preserving efficient vessel transit, upholding common fishery practices, and prioritizing safe Coast Guard search and rescue operations necessitates 1x1-nm corridors (W.F. Baird & Associates, 2019). Considering these constraints, wind plants will be densely packed into clusters.

Densely packed clusters produce wakes which adversely affect downwind turbines (Nygaard, 2014; Platis et al., 2018; Lundquist et al., 2019; Schneemann et al., 2020). Wakes are plumes downwind of turbines with slower wind speeds and increased turbulence. Mid-Atlantic wakes induced by large wind plants could impose wind speed deficits up to 2 m s^{-1} (Pryor et al., 2021; Golbazi et al., 2022). Wind speed deficits can be replenished by wake recovery in which turbulence entrains momentum from aloft into the waked zone (Stevens et al., 2016; Gupta and Baidya Roy, 2021). However, stably stratified conditions suppress mixing for wake recovery (Fitch et al., 2013; Vanderwende et al., 2016; Porté-Agel et al., 2020). Under certain conditions, mid-Atlantic wakes could propagate 100 km or more (Pryor et al., 2021; Golbazi et al., 2022; Stoelinga et al., 2022).

Wake characteristics have been evaluated using physics-based models of varying complexity. High-fidelity methods include computational fluid dynamics models solving Reynolds-Averaged Navier-Stokes (RANS) equations (Antonini et al., 2020), large-eddy simulations (LES) resolving the turbine rotor as an actuator disk (Mirocha et al., 2014; Aitken et al., 2014; Shapiro et al., 2019; Arthur et al., 2020), and mesoscale models parameterizing a hub-height momentum sink, sometimes including a turbulence source (Fitch et al., 2013; Volker et al., 2015; Archer et al., 2020; Gupta and Baidya Roy, 2021), as reviewed by Fischereit et al. (2022). Pryor et al. (2021) characterized mid-Atlantic wake impacts using mesoscale modeling of 55 simulation days. They examined modified wind plant layouts of 15-MW turbines under different flow scenarios, considering power densities between 2.1 and 4.34 MW km^{-2}. Stoelinga et al. (2022) estimated wake impacts using 15-MW turbines and 16 simulation days under typical southwesterly flow. Golbazi et al. (2022) considered summertime wakes with three scales of turbines to consider surface impacts. Finally, Rybchuk et al. (2022) addressed the sensitivity to wake characteristics under idealized conditions by varying planetary boundary layer (PBL) schemes.

Table 1. Summary of WRF simulations.

Simulation Type	Acronym	Turbine Type	Period	Added TKE Amount	# Turbines
No Wind Farms	NWF	N/A	09/2019-09/2020	N/A	0

https://doi.org/10.5194/wes-2023-38
Preprint. Discussion started: 4 May 2023

Vineyard Wind Only	VW_only	12 MW	09/2019-09/2020	0% and 100%	177
Lease Areas	LA	12 MW	09/2019-09/2020	0% and 100%	1,418
Call Areas	CA	12 MW	09/2019-11/2019 07/2020-09/2020	100%	3,219

In this work, we assess intra-plant and inter-plant wakes throughout the mid-Atlantic OCS using a year-long mesoscale modeling study. The simulations use the Weather Research and Forecasting Model (WRF) version 4.2.1 (Skamarock et al., 2019). One set of simulations runs with no wind farms (NWF) as a control, validated with lidar measurements, while the other uses the Fitch wind farm parameterization (WFP) (Fitch et al., 2012 with updates described by Archer et al. 2020) to incorporate turbine effects. Our simulations incorporate 12-MW turbines, similar to the 13-MW turbines to be installed at the Vineyard Wind lease area, and a power density of 3.14 MW km^{-2}. Simulations employ different wind plant layouts, including the Vineyard Wind Lease Area alone (VW_only), all lease areas (LA), and the lease areas plus the call areas (CA), to assess different waking scenarios (Table 1). We prioritize Vineyard Wind as the first lease area to begin construction. WFP simulations run separately by added turbulent kinetic energy (TKE) amount, including 0% added TKE (TKE_0) and 100% added TKE (TKE_100) to quantify the full range of uncertainty. NWF, VW_only, and LA simulations run from 01 September 2019 to 01 September 2020. Due to computational costs, CA simulations focus on the summertime stable period from 01 September to 31 October 2019 and 01 July to 31 August 2020 (Table 1). This time period highlights wake impacts during months with presumed frequent stable stratification and high electricity demands (Livingston and Lundquist, 2020) as a worst-case scenario.

The remainder of this paper is structured as follows: Section 2 introduces the model setup and configuration, model validation, and the analysis methods. Section 4 discusses variability in stratification, wakes, and power production. Section 5 concludes the work and offers recommendations for future work.

2 Methods

2.1 WRF Modeling Setup

We assess the effects of wakes and power production across the mid-Atlantic OCS using numerical weather prediction simulations with WRF version 4.2.1 and the WFP (Fitch et al., 2012). Version 4.2.1 allows for modification of the amount of TKE produced by turbines and ensures turbulence advection (Archer et al., 2020). Two nested domains comprise 6-km and 2-km horizontal resolutions (Pronk et al., 2022; Xia et al., 2022), respectively (Fig. 1). This same domain and period of study have been used to explore interactions between power production and sea breezes (Xia et al., 2022). Fine vertical resolution

(10 m) near the surface stretches aloft, with 17 levels within the lowest 200 m as recommended by Tomaszewski and Lundquist, (2020). We choose an 18-s time step in the outer domain, 54 vertical levels, a 5,000-Pa top, simple diffusion, and damping 6,000 m below the model top to prevent gravity wave reflection. Hourly 30-km initial and boundary conditions are provided by the European Centre for Medium-Range Forecasts (ECMWF) fifth generation reanalysis (ERA5) data set (Hersbach et al., 2020). Sea surface temperature is provided by the UK Met Office Operational Sea Surface Temperature and Sea Ice Analysis (OSTIA) data set (Donlon et al., 2012). We choose the Noah Land Surface Model (Niu et al., 2011), the Mellor-Yamada Nakanishi and Nino Level 2.5 PBL and surface layer (Nakanishi and Niino, 2006), New Thompson microphysics (Thompson et al., 2008), and the Rapid Radiative Transfer Model longwave and shortwave radiative transfer (Iacono et al., 2008) schemes. The Kain–Fritsch cumulus scheme parameterizes cloud microphysics in the outer domain only (Kain, 2004).

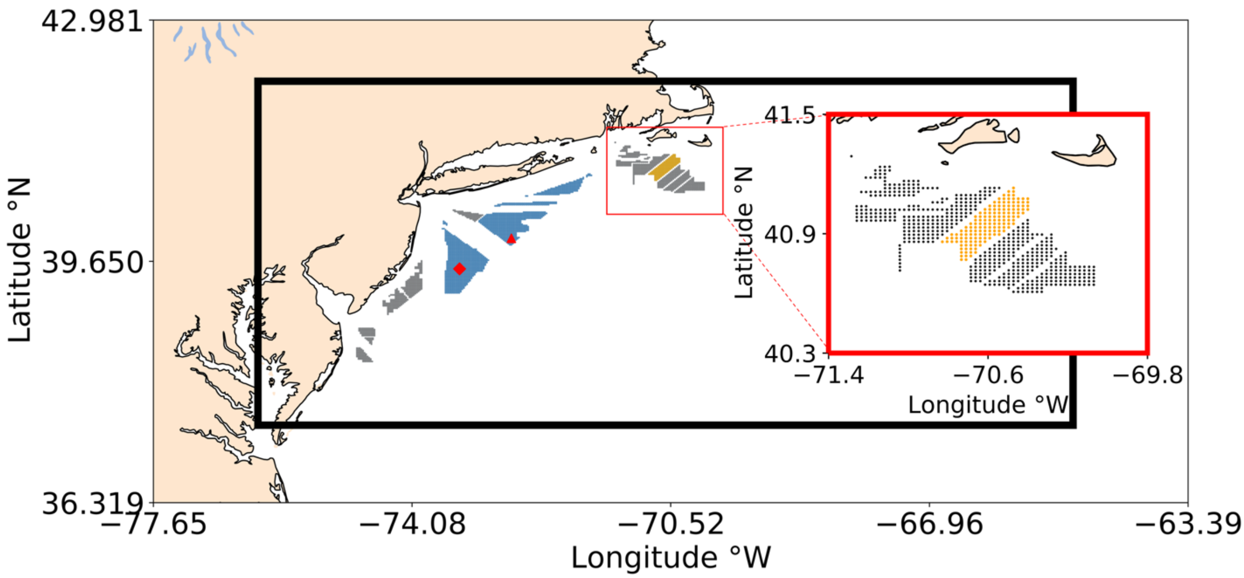

Fig. 1. Simulation domain 1 includes the entire region, and simulation domain 2 is outlined by the black rectangle. Each dot represents a wind turbine. Vineyard Wind is shown in orange, wind energy lease areas in gray, and call areas in blue. The red square is zoomed in on the Rhode Island/Massachusetts block of lease areas. E05 (red triangle) and E06 (red diamond) floating lidars are shown in red.

2.2 Wind Turbine Layouts

Wind turbines are sited within lease areas offshore of the U.S. East Coast (Fig. 1) as defined by the Bureau of Ocean Energy Management (BOEM, n.d.). Following realistic deployment strategies, we site individual turbines 1 nm, or 8.6 rotor diameters,

https://doi.org/10.5194/wes-2023-38
Preprint. Discussion started: 4 May 2023

apart and an additional 0.5 nm from lease area boundaries (W.F. Baird & Associates, 2019; Beiter et al., 2020; Musial W., personal communication, Sept. 2020). This layout provides a power density of 3.14 MW km^{-2}. Lower power densities in U.S. waters reflect wake concerns in Europe and the need to increase turbine spacing for wake replenishment. Areas that had already been approved for development are denoted as the lease areas (LA). Areas where competitive interest was yet to be determined are denoted as the call areas (CA). Both LA and CA are filled to spatial capacity with turbines (Fig. 1), recognizing renewable energy targets (218th Legislature, 2018).

2.3 Wind Turbine Characteristics

At the time of preparing this project, 12-MW turbines were speculated to be installed at Vineyard Wind. Since then, 13-MW turbines have been chosen for Vineyard Wind. For our simulations, we parameterize 12-MW turbines scaled from a 15-MW reference turbine with a 138-m hub height and 215-m rotor diameter. Power production increases between cut-in wind speed (3 m s^{-1}) and rated speed (11 m s^{-1}), region 2 of the power curve. Between rated and cut-out wind speed (30 m s^{-1}), region 3, an increase in wind speed no longer yields additional power production (Beiter et al., 2020) (Fig. 2a).

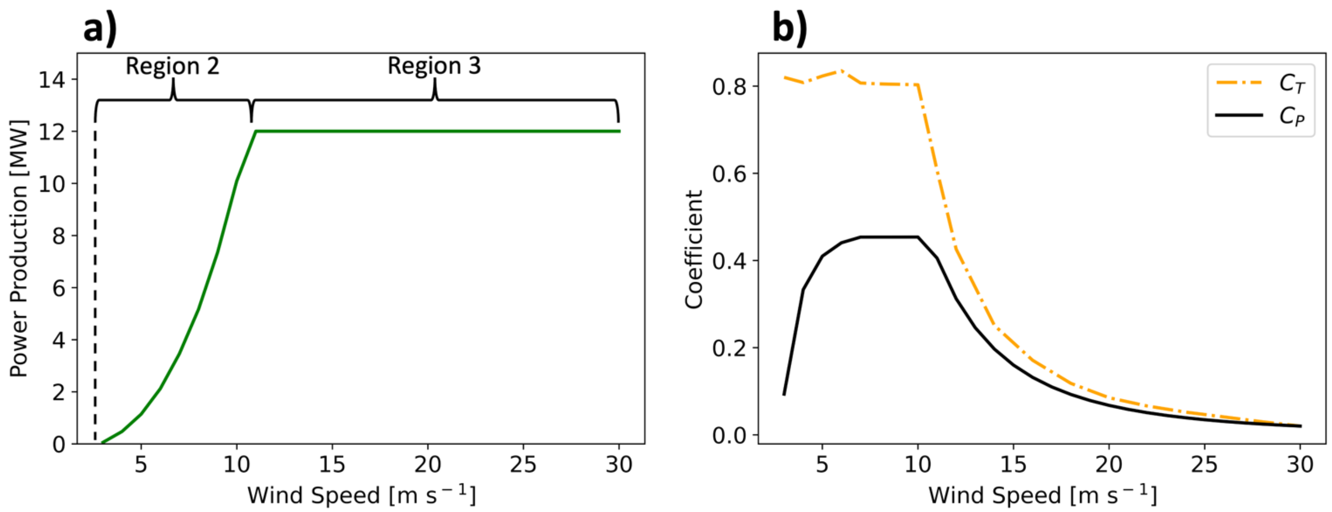

Fig. 2. Characteristics of the 12-MW scaled turbine used herein. (a) The power curve. (b) Curves showing the thrust coefficients (C_T, dashed orange) and the power coefficients (C_P, solid black) with wind speed across the *x*-axis.

2.4 Wind Farm Parameterization

We use the WFP (Fitch et al., 2012) to incorporate the effects of wind turbines on the 2-km grid. Horizontal wind speed reduction from turbine drag (Eq. 1), power production (Eq. 2), and turbulence generation (Fitch et al., 2012; Archer et al., 2020) (Eq. 3) are calculated in the WFP from:

$$\frac{\delta|\mathbf{V}|_{ijk}}{\delta t} = -\frac{N_{ij}C_T(|\mathbf{V}|_{ijk})|\mathbf{V}|_{ijk}^2A_{ijk}}{2(z_{k+1}-z_k)} \tag{1}$$

$$\frac{\delta P_{ijk}}{\delta t} = \frac{N_{ij}C_P(|\mathbf{V}|_{ijk})|\mathbf{V}|_{ijk}^3A_{ijk}}{2(z_{k+1}-z_k)} \tag{2}$$

$$\frac{\delta TKE_{ijk}}{\delta t} = \frac{N_{ij}C_{TKE}(|\mathbf{V}|_{ijk})|\mathbf{V}|_{ijk}^3A_{ijk}}{2(z_{k+1}-z_k)} \tag{3}$$

where i, j, and k represent Cartesian model coordinates, $C_T(|\mathbf{V}|_{ijk})$ is the wind-speed-dependent thrust coefficient, $|\mathbf{V}|$ is the wind speed at turbine hub height, ρ is the air density, A_{ijk} is the rotor swept area, N_{ij} is the number density of turbines in grid cell ij, $C_P(|\mathbf{V}|_{ijk})$ is the wind-speed-dependent power coefficient, z_k is the height of vertical model level k, and C_{TKE} is the fraction of energy converted to TKE (Fitch et al., 2012). These values are calculated at each model level, as the use of a rotor-equivalent wind speed generally exerts a minor effect (Redfern et al., 2019).

The thrust and power coefficients (C_T and C_P, respectively) vary with wind speed as defined by wind turbine manufacturers (Fig. 2b). The thrust coefficient C_T is the non-dimensionalized thrust force exerted by wind on the rotor-swept plane (Burton et al., 2011).

The power coefficient C_P governs the fraction of rotor kinetic energy converted into electrical power. This conversion is not perfectly efficient due to electrical and mechanical losses (Fitch et al., 2012; Archer et al., 2020). The leftover fraction of energy (Eq. 4) from the difference between C_T and C_p is transformed into turbulence, C_{TKE}.

$$C_{TKE} = C_T - C_P \tag{4}$$

Because electromechanical losses are not represented by the WFP, all leftover energy converts to TKE, and so the TKE may be overestimated (Fitch et al., 2012; Archer et al., 2020). Some researchers suggest this TKE term is unnecessary (Volker et al., 2015), although comparisons to large-eddy simulations (Vanderwende et al., 2016) and observations (Siedersleben et al., 2020) suggest the turbine-produced TKE is critical to include. Any overestimation of TKE would enhance turbulent mixing, thereby exaggerating turbulent transport of momentum that causes wake recovery, and overestimating power production. Therefore, Archer et al. (2020) propose reducing C_{TKE} to 25%. For these simulations, we bound this uncertainty by carrying out simulations with 100% and 0% added TKE (Fig. A1). Turbulence advection is turned on.

https://doi.org/10.5194/wes-2023-38
Preprint. Discussion started: 4 May 2023

2.5 Observations

The NWF simulation is compared to observations of offshore wind profiles. Two buoy-mounted metocean observing systems, denoted E05 and E06, are located within the Hudson North and Hudson South Call Areas of the New York Bight (Fig. 3). Each buoy system samples line-of-sight boundary-layer wind speed and wind direction using the ZephIR ZX300M light detection and ranging (lidar) instrument. The lidars are mounted 2 m above the sea surface and take measurements at 20-m intervals up to 200 m, providing 10-min averages of wind speed and direction, which the New York State Energy Research and Development Authority (NYSERDA) has made publicly available (DNV, 2022). We use floating lidar data to validate simulations for 01 September 2019 to 01 September 2020.

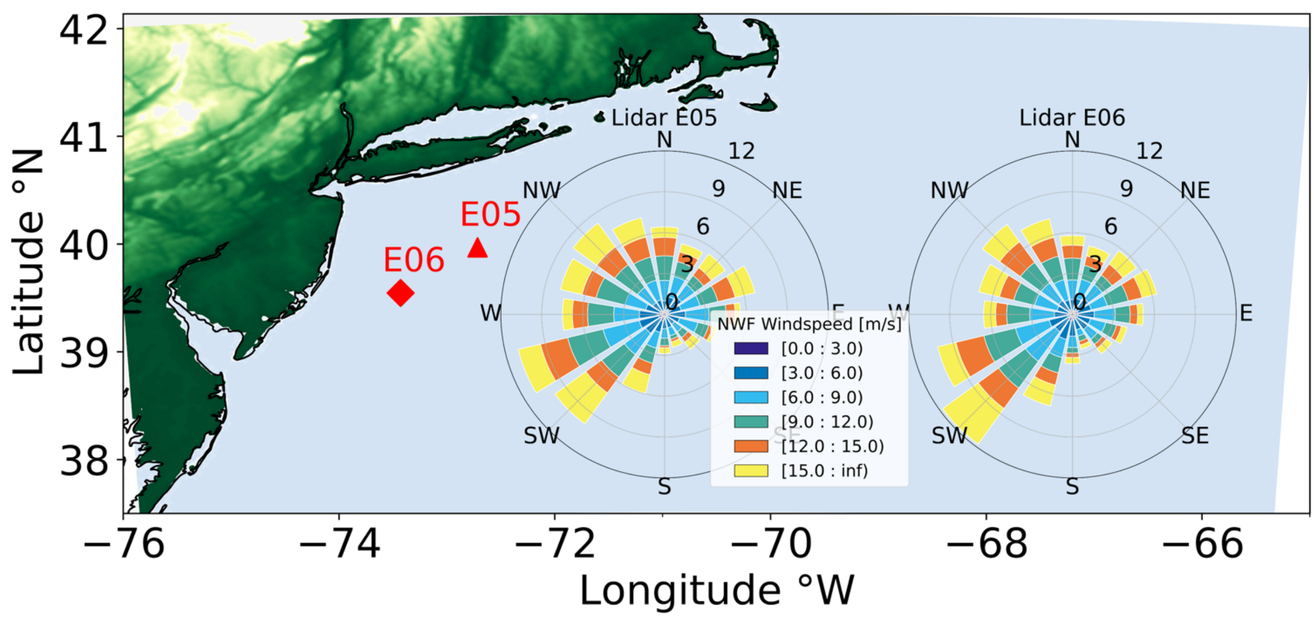

Fig. 3. Hub-height wind roses for the NYSERDA Hudson North (E05) and Hudson South (E06) floating lidars during the period 01 September 2019 to 01 September 2020. E06 is shown as the red diamond and E05 as the red triangle.

2.6 Model Validation

We validate the NWF model by comparing wind speed estimated by the turbine-free simulations with observations from E05 and E06 lidars. Model output is obtained from the grid cells containing the lidars in 20-m intervals from 60 m to 200 m

https://doi.org/10.5194/wes-2023-38
Preprint. Discussion started: 4 May 2023

following Pronk et al. (2022). Wind speeds and directions are compared using a suite of metrics (Eq.s 5-7) including the correlation coefficient (CC), centered root-mean-square error (cRMSE), and bias:

$$\mathrm{CC} = \frac{\sum_i^N (V_{WRF_i} - \overline{V_{WRF}})(V_{lidar_i} - \overline{V_{lidar}})}{N\sigma_{WRF}\sigma_{lidar}} \tag{5}$$

$$\mathrm{cRMSE} = \sqrt{\frac{\sum_i^N \left((V_{WRF_i} - \overline{V_{WRF}}) - (V_{lidar_i} - \overline{V_{lidar}})\right)^2}{N}} \tag{6}$$

$$\mathrm{Bias} = \frac{\sum_i^N (V_{WRF_i} - V_{lidar_i})}{N} \tag{7}$$

where V is the wind speed, N is the total number of values, and σ is the standard deviation. Earth mover's distance (EMD), or the Wasserstein metric, is calculated with a SciPy function (Virtanen et al., 2020) as in other wind resource evaluations (Hahmann et al., 2020). Time stamps in which the lidar returns NaN values are removed from WRF data sets during comparison. Doing so removes 8.1% and 13.6% of wind speed data at 140 m at E05 and E06, respectively. A CC value of one indicates a perfect correlation between NWF and lidar values. A value of 0 for cRMSE indicates that all values lie on the 1:1 regression line. Negative biases indicate an underestimation from WRF. A value of 0 for EMD indicates that probability density functions from each data source are equivalent.

https://doi.org/10.5194/wes-2023-38
Preprint. Discussion started: 4 May 2023

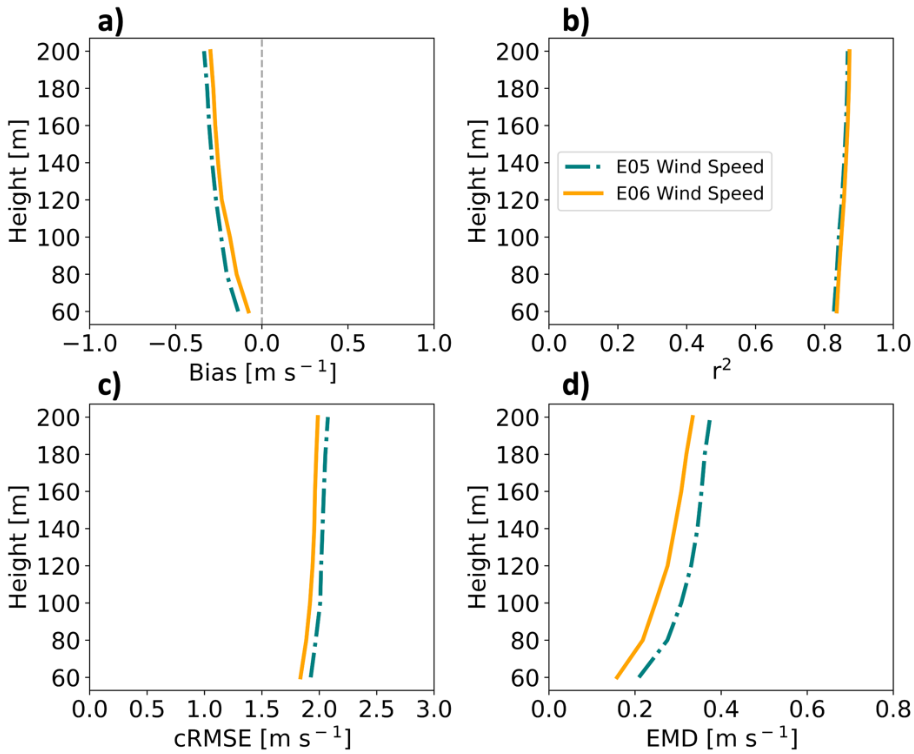

Fig. 4. Vertical profiles for wind speed comparative metrics at the E05 (teal) and E06 (orange) lidars from 01 September 2019 to 01 September 2020. Shown are (a) bias, (b) correlation, (c) centered root-mean-square error, and (d) earth mover's distance.

NWF wind speed profiles are compared with lidar observations for the period 01 September 2019 to 01 September 2020 to assess model skill (Fig. 4). Note that Pronk et al. (2022) provide validation metrics against the E05 lidar profile during the same period of study and find similar results. Negative biases increase in magnitude with height between 0 m s^{-1} and −0.5 m s^{-1} (Fig. 4a), showing the model underestimates the wind speed. Strengths of variation among WRF output and the lidars range between 0.82 and 0.86 (Fig. 4b). Centered RMSE increases with height around 2 m s^{-1} (Fig. 4c). Finally, EMD values originate around 0.2 m s^{-1} at 60 m and increase with height (Fig. 4d). Comparing lidars E05 and E06, WRF performs better at E06 with a smaller bias by 0.04 m s^{-1}, lower cRMSE by 0.08 m s^{-1}, better correlation by 0.003, and smaller EMD by 0.05 m s^{-1}.

https://doi.org/10.5194/wes-2023-38
Preprint. Discussion started: 4 May 2023

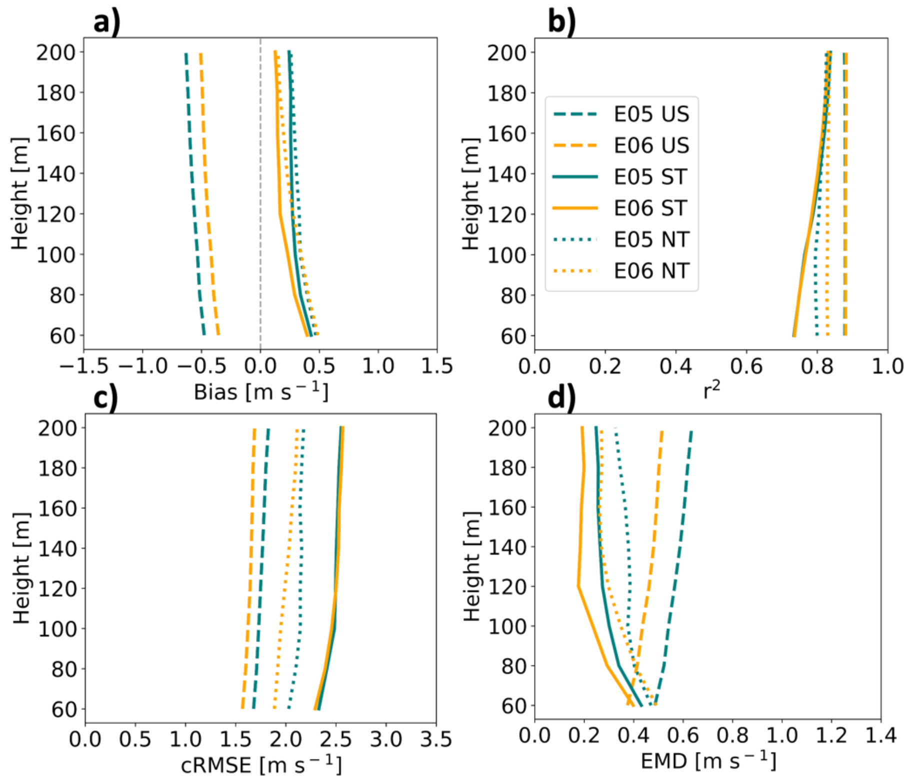

Fig. 5. Vertical profiles for wind speed comparative metrics at the E05 (teal) and E06 (orange) lidars subset by stratification (US = unstable, ST = stable, NT = neutral). Shown are (a) bias, (b) correlation, (c) centered root-mean-square error, and (d) earth mover's distance.

We further assess the NWF performance by stability conditions. In unstable stratification, WRF wind speeds have negative bias that gradually increases in magnitude with height from −0.5 m s^{-1} at 60 m (Fig. 5a). In stable and neutral conditions, WRF overestimates wind speed by roughly 0.5 m s^{-1} at 60 m with smaller biases higher (Fig. 5a). Comparing between E05 and E06 profiles, WRF performs better at the E06 lidar location by 0.1 m s^{-1} in unstable conditions, 0.08 m s^{-1} in stable conditions, and 0.05 m s^{-1} in neutral conditions.

NWF and lidar wind speeds correlate well. Correlation remains largest in unstable conditions for all heights (Fig. 5b). The worst strength of relationship occurs in stable stratification although there is improvement aloft, and by 160 m, correlation between stable and neutral conditions is largely equivalent (Fig. 5b). On average, WRF performance is the same in unstable and stable conditions and better at E06 by 0.02 in neutral conditions.

https://doi.org/10.5194/wes-2023-38
Preprint. Discussion started: 4 May 2023

Centered RMSE profiles change with stratification. In unstable conditions, cRMSE increases somewhat with height originating from greater than 1.5 m s^{-1} at 60 m (Fig. 5c). In stable stratification, the cRMSE profile begins at roughly 2.3 m s^{-1} at 60 m and increases with height. In neutral conditions, cRMSE increases with height from around 2 m s^{-1}. As before, WRF performs better at E06. On average, cRMSE is lower at E06 by 0.1 m s^{-1} in unstable conditions, by a negligible amount in stable conditions, and by 0.1 m s^{-1} in neutral conditions.

Earth mover's distance has more variability with height. EMD is largest in unstable stratification, increasing with height from roughly 0.5 m s^{-1} at 60 m (Fig. 5d). In stable conditions, EMD decreases with height and originates at slightly greater than 0.4 m s^{-1} at 60 m. In neutral stratification, EMD decreases with height from slightly greater than 0.4 m s^{-1}. On average, WRF performs better at E06 by 0.1 m s^{-1} in unstable conditions, by 0.06 m s^{-1} in stable conditions, and by 0.05 m s^{-1} in neutral conditions.

2.7 Stability Classification

Different methods can be used to identify stratification, or atmospheric stability. Stable stratification can occur in coastal regions when warm air advects over a cooler sea surface, thereby suppressing buoyancy and turbulent mixing. Likewise, unstable stratification can occur when cool air advects over a warmer sea surface. Some observations suggest more frequent unstable stratification, based on the Obukhov length (Archer et al., 2016). The sign of the Obukhov length depends on the sign of heat flux and can be a useful metric for determining stability conditions. Other observations suggest that minimal turbulence and strong veer can be characteristic of stable conditions (Bodini et al., 2019). Wind veer increases in stable stratification as the influence of buoyant turbulence-induced friction reduces. Thus, winds turn to approach quasi-geostrophic flow at a quicker rate which can be further exaggerated by the presence of a low-level jet.

Here we obtain the WRF-output Obukhov length (Monin and Obukhov, 1954) (L), representative of the height at which buoyant production of turbulence first dominates mechanical shear production of turbulence (Eq. 8):

$$L = -\frac{u_*^3 \overline{\theta_v}}{\kappa g \left(\overline{w'\theta_v'}\right)} \tag{8}$$

where u_* is the friction velocity, θ_v is the virtual potential temperature, κ is the von-Karman constant of 0.4, g is gravitational acceleration, and $\overline{w'\theta_v'}$ is the vertical turbulent heat flux. Lengths between 0 m and −1,000 m are characterized as unstable stratification and lengths between 0 m and 1,000 m are categorized as stable stratification. Lengths approaching negative or positive infinity are neutral. Each timestamp from the NWF run is assigned a stability for the period 01 September 2019 to 01 September 2020 at a grid point centered on Vineyard Wind.

https://doi.org/10.5194/wes-2023-38
Preprint. Discussion started: 4 May 2023

2.8 Wake Identification

The wake delineates the region downwind of turbines with a velocity deficit and turbulence enhancement. We identify the wind speed wake deficit by subtracting NWF wind speeds from WFP wind speeds at the hub height. Averaging across all times during the period 01 September 2019 to 01 September 2020 identifies the overall mean wake wind speed. Because wakes typically propagate to the northeast (Fig. 3), we calculate the propagation distance of wakes under various conditions along a line extending northeast of Vineyard Wind and report the distance along the line where wake wind speeds reach a threshold. The threshold of -0.5 m s^{-1} is chosen following Golbazi et al., (2022); Rybchuk et al., (2022). Finally, we define the areal extent of wakes as the area with a wind speed deficit less than -0.5 m s^{-1}.

2.9 Grid Balancing

We compare model-output energy production with New England grid demand. Demand data are provided hourly (NEISO, 2023a). For comparison, we compute hourly averages of WFP power production from each set of simulations. We compare with the national energy supply by acquiring the total from the U.S. Energy Information Administration (EIA, 2023).

2.10 Power Variability

Assessing power variability is essential for addressing temporally changing grid demands. We assess the differences in electricity generation by deployment scenario through collecting power output from grid cells containing turbines separately from VW_only, LA, and CA simulations. This method is performed separately by added TKE amount. Power is summed across grid cells containing turbines and averaged at 1-day, 7-day, and 30-day intervals for comparison. We address seasonal and diurnal variability by further separating and averaging power production totals at each timestep into bins by month and hour of day.

$$Loss_{external} = 100 - \left(\frac{P_{VW_{waked}}}{P_{VW_{only}}}\right) * 100\% \tag{9}$$

$$Loss_{internal} = 100 - \left(\frac{P_{VW_{only}}}{P_{NWF}}\right) * 100\% \tag{10}$$

Cluster-induced power deficits at Vineyard Wind occur due to external wakes from the upwind lease and call areas. Power output from VW_only, LA, and CA simulations are averaged in hourly windows at grid cells containing Vineyard Wind turbines to reduce the effects of numerical noise. The resulting power averages from LA and CA simulations are divided by the averages from VW_only at each timestamp. The hour of day and month of year categorize each timestamp and percentages are placed into bins accordingly. Within each bin the percentages are averaged. Only power production totals greater than 9.9 MW are considered when calculating power losses. This threshold represents the power production total when all turbines

https://doi.org/10.5194/wes-2023-38
Preprint. Discussion started: 4 May 2023

within Vineyard Wind begin operation at the cut-in wind speed. For reference, the total power production for Vineyard Wind at rated power is 2,124 MW. This method is repeated separately for TKE_0 and TKE_100 runs.

Individual turbines generate internal wakes within the Vineyard Wind plant that adversely affect power production. To quantify internal wake effects at Vineyard Wind, we collect NWF wind speeds at the hub height in each cell containing Vineyard Wind turbines. Wind speeds are convolved with the power curve and scaled by the number of turbines per cell at 0.01 m s^{-1} intervals. This method returns the amount of power that Vineyard Wind would produce in the absence of wakes. Hourly power averages are obtained from both NWF and VW_only runs and considered only if power production exceeds 9.9 MW. VW_only power totals are divided by the NWF power estimations from the power curve. Again, each timestamp is categorized by hour of day and month of year, and percentages are binned for averaging. These steps are repeated for both TKE_0 and TKE_100 runs.

3 Results

3.1 Year-Round NWF Stratification

The predominance of NWF stability conditions changes throughout the year (Fig. 6, Fig. 7) as assessed using the Obukhov Length (L) centered at Vineyard Wind.

https://doi.org/10.5194/wes-2023-38
Preprint. Discussion started: 4 May 2023

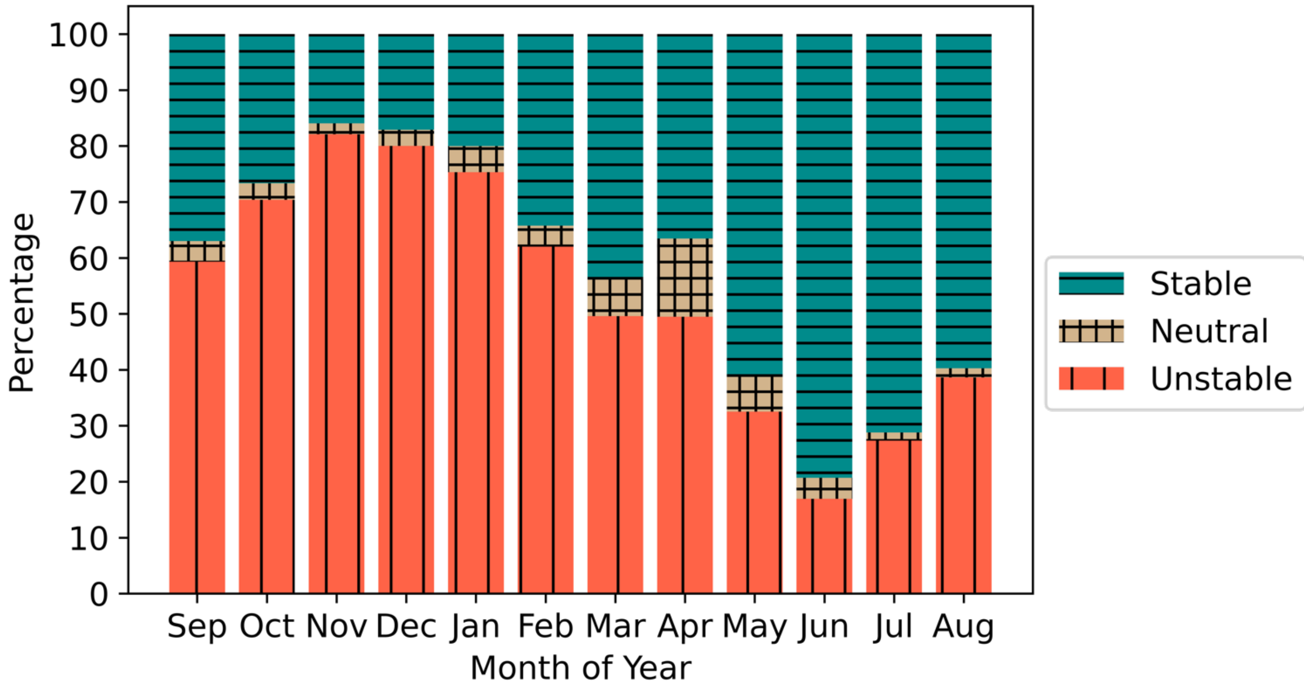

Fig. 6. Stability classification using the Obukhov length for the period 01 September 2019 to 01 September 2020 at Vineyard Wind from NWF. Tan crosshatch represents neutral stratification, teal horizontal lines are stable stratification, and red vertical lines are unstable stratification.

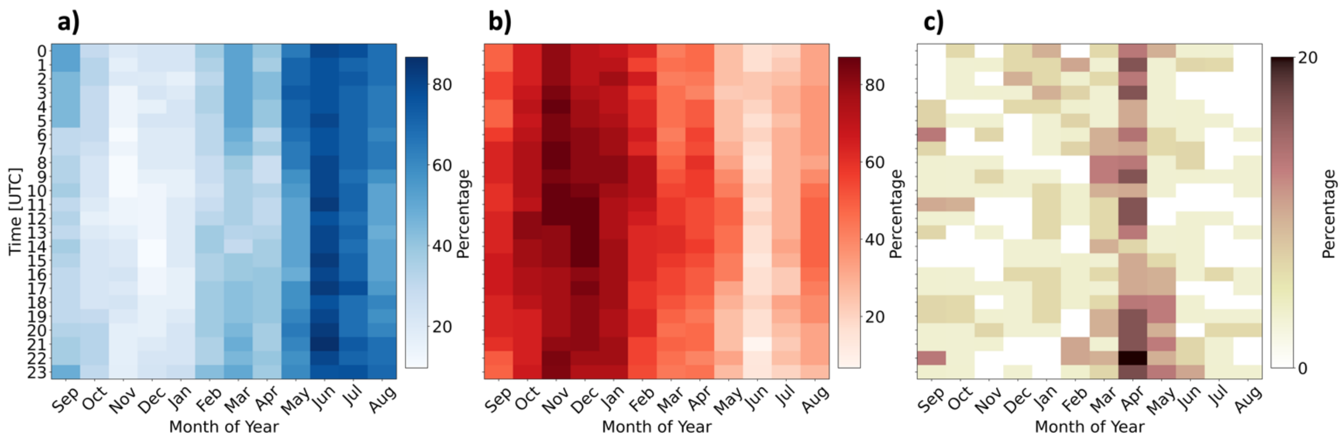

Fig. 7. Percentages of occurrence for (a) stable stratification, (b) unstable stratification, and (c) neutral stratification from 01 September 2019 to 01 September 2020.

https://doi.org/10.5194/wes-2023-38
Preprint. Discussion started: 4 May 2023

The winter features predominant unstable stratification while the summer features frequent stable stratification (Bodini et al., 2019; Optis et al., 2020) (Fig. 6, Fig. 7). The strong stability in summer is caused by nearby surface-heated air advecting over the colder OCS. These dynamics reverse during winter when cold air from land advects over warmer water. Overall, stratification is most frequently unstable during November and stable during June. April features the greatest percentage of neutral conditions as the springtime transition from cooler to warmer air reduces the air-sea temperature gradient. The same pattern occurs elsewhere throughout variability in stratification is weaker than the seasonal cycle (Fig. 7). The mean unstable, stable, and neutral percentages of occurrence at Vineyard Wind are 53.6%, 41.9%, and 4.5%, respectively, for the period 01 September 2019 to 01 September 2020, and stability calculations from the model grid cells that house lidars E05 and E06 reveal similar results (Fig. B1). However, L may not always represent conditions aloft (Fig. C1).

3.2 Wake Variability

Here, we categorize wakes by the maximum wind speed deficit, the spatial extent, and the downwind propagation distance. While wakes remain relatively unchanged between TKE_0 and TKE_100, they drastically vary by stratification. The maximum average wake wind speed deficit intensifies from -1.5 m s^{-1} to -2.8 m s^{-1}, moving from unstable to stable conditions for TKE_100 (Fig. 8a,c). Normalized with mean NWF hub-height wind speeds of 9.2 m s^{-1} (unstable) and 11.6 m s^{-1} (stable), the corresponding mean wind speed deficits are 16% and 24%. Similarly, the maximum average wind speed deficit intensifies from -1.8 m s^{-1} to -3.2 m s^{-1}, a normalized reduction of 19% and 27%, moving from unstable to stable at TKE_0 (Fig. 8b,d). Thus, reducing TKE from 100% to 0% has a smaller impact on wake strength than increasing stability. While here we address the uncertainty introduced by varying the added TKE, Rybchuk et al. (2022) address uncertainty introduced by varying planetary boundary layer (PBL) schemes.

The areal extent of wakes changes by stability and added TKE. Wake deficits stronger than the -0.5 m s^{-1} cutoff in unstable stratification at TKE_100 (Fig. 8a) cover a total area of 7,296 km^2 and represent the best-case scenario where wakes impact the smallest area. In stable stratification at TKE_100 (Fig. 8c), wakes cover a larger area of 16,404 km^2, or 2.2 times larger. A similar increase occurs using TKE_0, although areal coverage is larger from reduced wind speed replenishment. At TKE_0 in unstable conditions (Fig. 8b), wakes stronger than -0.5 m s^{-1} cover an area of 7,952 km^2. In stable stratification, the area increases to 16,060 km^2 (Fig. 8d), a factor of 2. The spatial extent of strong wakes spreading furthest throughout the region, representing the worst-case scenario, occurs in stable conditions at TKE_0. Wakes interact between immediate wind plant neighbors for all scenarios.

https://doi.org/10.5194/wes-2023-38
Preprint. Discussion started: 4 May 2023

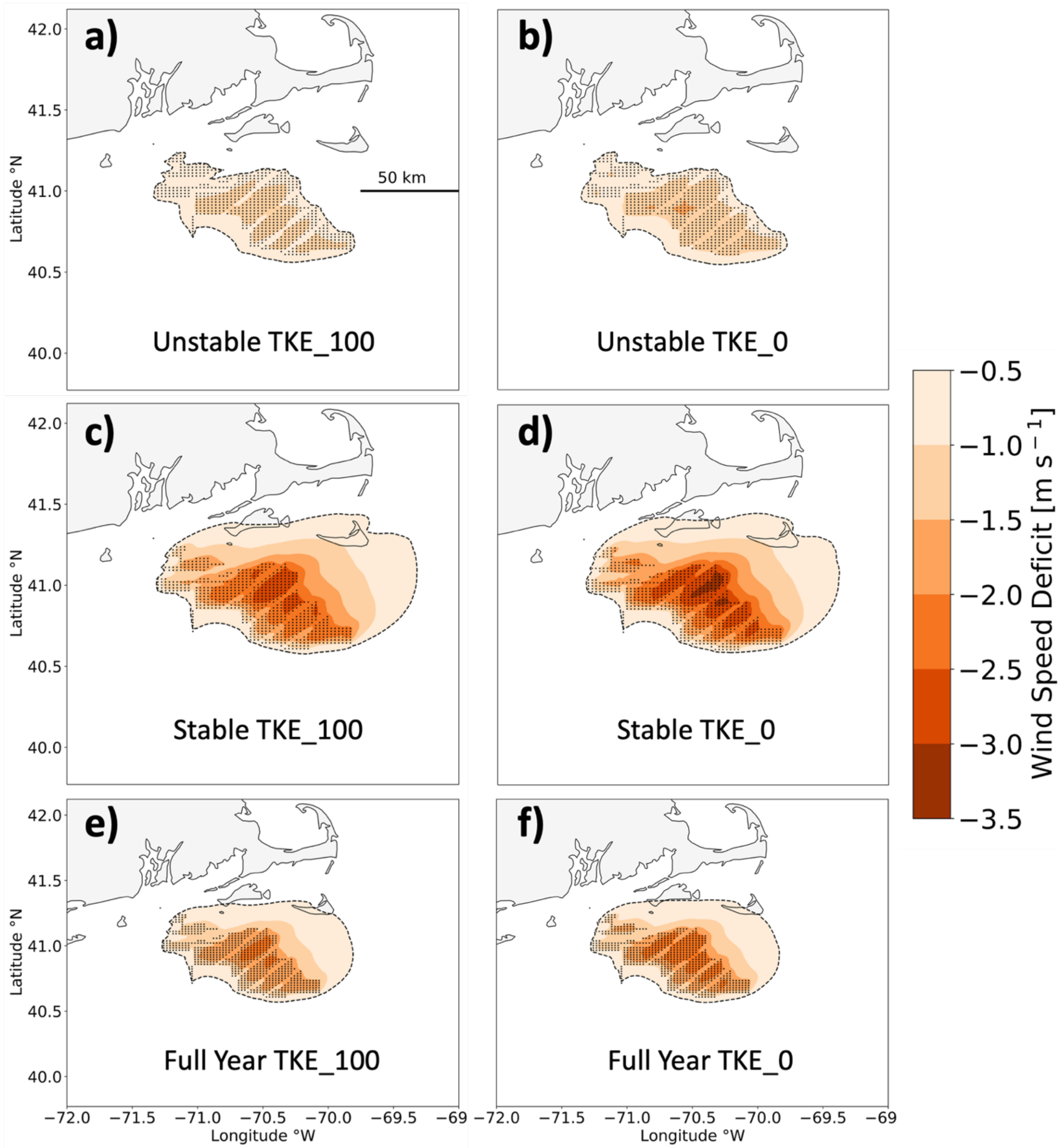

Fig. 8. Average wake wind speeds among the lease areas during (a,b) unstable stratification, during (c,d) stable stratification, and (e,f) the full period 01 September 2019 to 01 September 2020. Wakes are simulated with 100% added TKE (a,c,e) or 0% added TKE (b,d,f). Wind speed deficits are shown by the colored contouring, and turbines are shown as the black dots. The −0.5 m s^{-1} threshold is outlined by the black dashed line.

https://doi.org/10.5194/wes-2023-38
Preprint. Discussion started: 4 May 2023

Stratification exerts a stronger effect on wake propagation distance than does TKE. For instance, wakes extending 1 km downwind in unstable conditions reach 58 km in stable conditions at TKE_100 (Fig. 8a,c), similar to the estimate of 50 km from Golbazi et al. (2022). Likewise, wake deficits reaching 3 km downwind in unstable stratification reach 55 km downwind in stable stratification at TKE_0 (Fig. 8b,d). Overall, altering the added TKE amount has a small impact on the propagation distance of wakes relative to stratification, and combining stable stratification with TKE_0 results in the strongest wakes.

Yearly averaged wakes show similar trends with TKE and stability. The maximum wake strength intensifies from -2.2 m s^{-1} to -2.5 m s^{-1} moving from TKE_100 to TKE_0 (Fig. 8e,f). Reducing TKE also increases the spatial coverage of wakes from 13,040 km^2 using TKE_100 (Fig. 8e) to covering 13,268 km^2 using TKE_0 (Fig. 8f). Downwind propagation distances remain similar over the yearlong period with wakes reaching 43 km at TKE_100 and 41 km at TKE_0.

Reduced TKE limits turbulence-induced momentum transport from aloft, thereby increasing wake strength. Counter-intuitively, longer-lasting wakes in TKE_100 develop from a larger reduction in momentum from wake recovery above the turbines, leaving less momentum available for replenishment downwind. The same patterns exist for VW_only and CA (Fig. D1) wakes.

3.3 Power Deficits

3.3.1 External Wake Losses

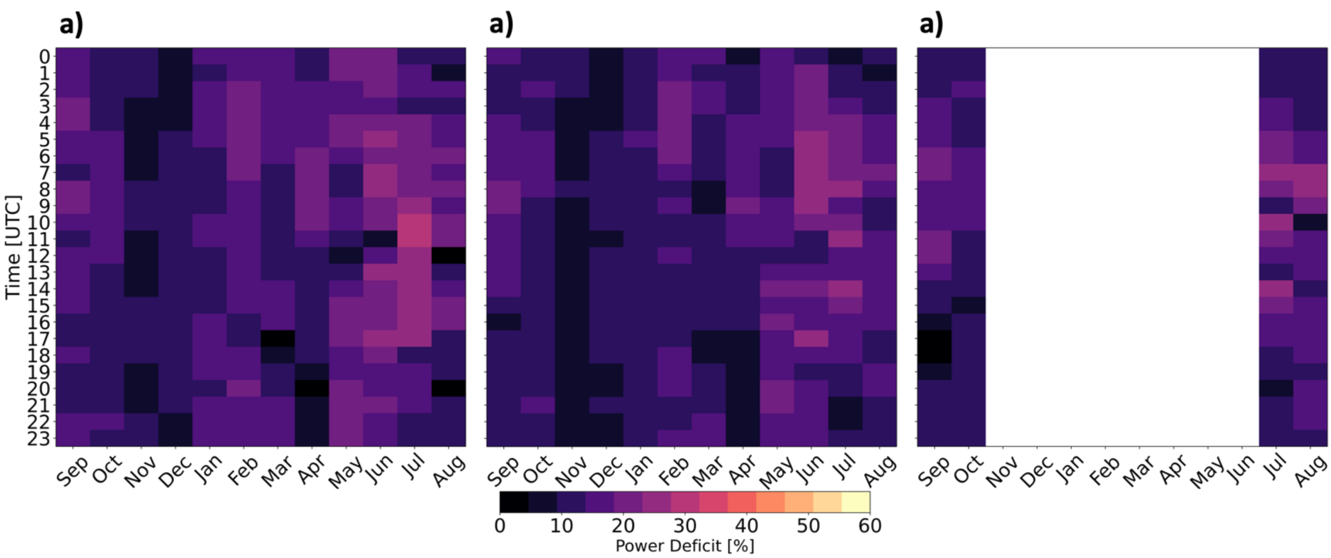

Fig. 9. The power deficit at Vineyard Wind when waked by (a) the LA at TKE_0, (b) the LA at TKE_100, and (c) the CA at TKE_100. The color bar is broad to facilitate comparison with losses in Fig. 10.

https://doi.org/10.5194/wes-2023-38
Preprint. Discussion started: 4 May 2023

Vineyard Wind experiences power deficits due to external wakes from the LA and the CA (Eq. 9). Considering external wakes from the LA at TKE_0, the average yearlong power deficit at Vineyard Wind is 14.7% (Fig. 9a). When Vineyard Wind is waked by the LA at TKE_100, the average yearlong power deficit reduces to 13.4% (Fig. 9b) because increased turbulence supports faster replenishment. When incorporating wakes from the CA (at TKE_100), the mean Vineyard Wind power deficit (over four months) is 14.3% (Fig. 9c). However, power losses vary as larger reductions from external wakes occur during summer while smaller reductions occur during winter.

External wake-induced losses vary both diurnally and seasonally. Larger power deficits occur more often during summer due to stable stratification (Fig. 6, Fig. 7a). Smaller power deficits occur during winter (Fig. 9), with faster winds that exceed rated wind speed and unstable conditions that erode wakes faster. Larger power deficits correspond with stable stratification in June and July. Conversely, smaller power deficits occur with unstable stratification throughout November and December. These patterns occur because of advection of colder air over warmer water in winter which cause unstable conditions that erode wakes faster. Conversely, warmer air advects over colder water during the summer, inducing stable conditions which limit turbulent wake recovery.

https://doi.org/10.5194/wes-2023-38
Preprint. Discussion started: 4 May 2023

eawe european academy of wind energy
Open Access WIND ENERGY SCIENCE DISCUSSIONS

3.3.2 Internal Wake Losses

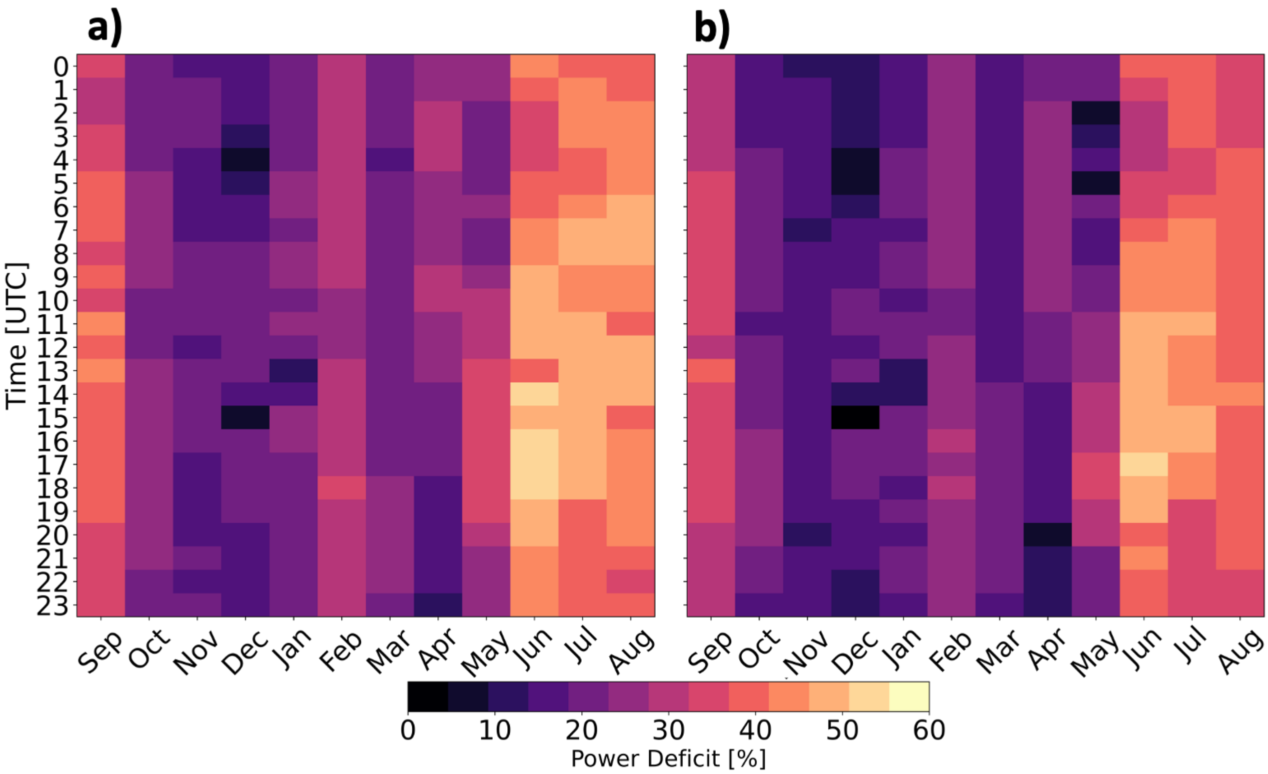

Fig. 10. The percentage of power loss at Vineyard Wind from internal wakes at (a) TKE_0 and (b) TKE_100.

375

Internal power deficits (Eq. 10) at Vineyard Wind are at least 25% stronger than externally induced power deficits but experience similar variability with stability and TKE amount (Fig. 10). Internal waking induces weaker deficits during winter and stronger deficits during summer. As with external wakes, a clear diurnal pattern fails to emerge. Yearlong internal wakes from TKE_0 and TKE_100 induce power losses of 29.2% and 25.7%, respectively. Using different PBL schemes with similar turbine spacing under steady-state idealized conditions, Rybchuk et al. (2022) find similar internal losses to capacity factor, up to 31.6%.

The average yearlong power deficit at Vineyard Wind considering both TKE amounts, internal wakes, and external wakes from the LA is 35.9%. These results concur with wake-induced losses found by Pryor et al. (2021) of 35.3% among the LA, based on 11 5-day periods of different flow scenarios. Observations of wake-induced power losses have large variability over the year, ranging from as low as 5% to as high as 40% (Lee and Fields, 2021). Overall, external wakes produce yearly averaged

https://doi.org/10.5194/wes-2023-38
Preprint. Discussion started: 4 May 2023

power losses of 14.1%, while internal wakes induce larger losses of 27.4%. Thus, we stress the importance of resolving region-specific and time-varying wakes for accurate energy prediction estimates.

3.4 Annual Energy Production

Predictions of energy supply are critical for planning, operations, and diversification of renewables. Without internal or external wake effects, Vineyard Wind would produce 11.61 TWh and meet 10.02% of New England's average demand. Annual energy production (AEP) from VW_only, considering just internal wakes, reduces to 9.19 TWh (TKE_0) or 9.55 TWh (TKE_100) which could meet 7.94% to 8.24% of New England's demand. Including both internal and external wakes from the LA, Vineyard Wind would produce 8.19 TWh (TKE_0) or 8.65 TWh (TKE_100), meeting 7.07% to 7.47% of demand.

Increasing the number of turbines increases the demand fulfilled; AEP from the LA is 68.12 TWh (TKE_0) or 70.9 TWh (TKE_100), supplying 58.82% to 61.22% of New England's demand. On an hourly basis, the LAs fulfill demand only 24.6% (TKE_0) and 26.5% (TKE_100) of the time, highlighting the necessity for resolving accurate wake losses across the OCS. Previous work (Livingston and Lundquist, 2020) assuming a constant 20% wake loss, shown here to be underestimated, suggested that 2,000 10-MW turbines could meet New England's demand 37% of the time. In all, the LA, with 1,418 12-MW turbines, supply 68 TWh year^{-1} and 71 TWh year^{-1}, or 1.72% (TKE_0) to 1.65% (TKE_100) of the nation's energy supply.

3.5 Power Variability by TKE Amount

3.5.1 Temporal Power Variability

While differences in wake strength between TKE amounts alter power production, wind speed exerts a larger influence. Maximum power is produced during spring with the least amount of power produced during summer (Fig. 11a) for both TKE_0 and TKE_100, because spring features faster wind speeds (Fig. 11b). Power production responds to hub-height wind speeds (Fig. 11) more than stability conditions (Fig. 6, Fig. 7). Reduced power production during summer may be problematic as New England's top-10 utility demand days since 1997 have all occurred in July or August (NEISO, 2023b).

https://doi.org/10.5194/wes-2023-38
Preprint. Discussion started: 4 May 2023

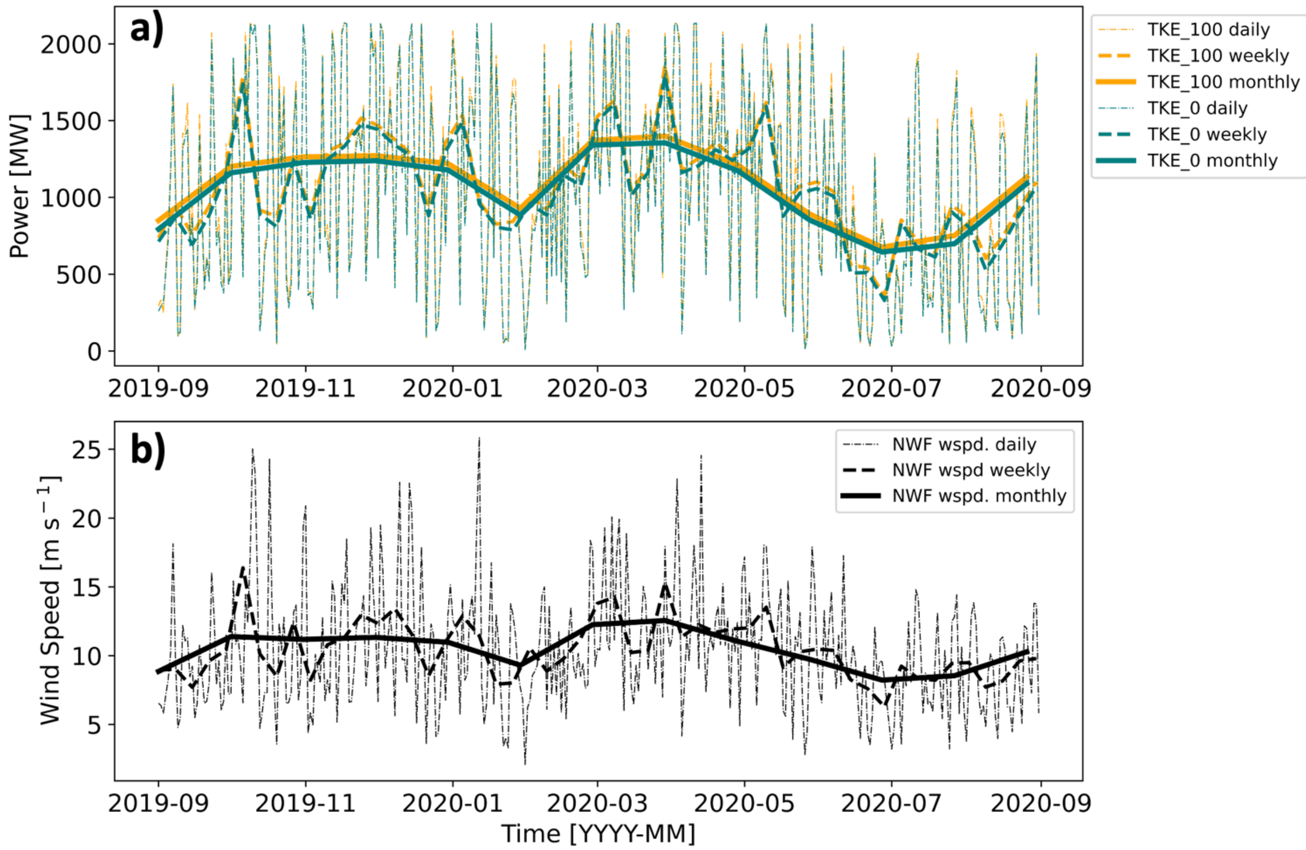

Fig. 11. (a) Total power production at Vineyard Wind by TKE amount. TKE_100 power output is shown in orange and TKE_0 output is shown in teal. (b) Hub-height NWF wind speed at a point centered on Vineyard Wind. Dotted lines represent the daily average, dashed lines the 7-d average, and solid lines the 30-d average.

Total power production varies slightly between TKE_100 and TKE_0. Due to weaker replenishment within the rotor-swept area, TKE_0 wakes are stronger, so TKE_0 produces less total power than TKE_100 (Fig. 11a). Over the year, TKE_0 runs produce 96.2% (VW_only) and 96.1% (LA) of the power of TKE_100. This difference does not arise from extreme outliers, as TKE_0 runs produce less power more frequently, at 71.3% (VW_only) or 81.2% (LA) of the time.

https://doi.org/10.5194/wes-2023-38
Preprint. Discussion started: 4 May 2023

3.5.2 Power Variability by Wind Speed

Differences in power production (TKE_100 − TKE_0) vary by NWF hub-height wind speed (Fig. 12). These differences are small at slow wind speeds, because little momentum is available for wake recovery, and at faster wind speeds within region 3 of the power curve (11−30 m s^{-1}) where wind speed changes do not affect power production. Differences in wind speed within region 3 should have no effect on power production and are caused by numerical noise propagating through Vineyard Wind (Fig. E1). The largest differences in power production occur in region 2 and around rated wind speed where the power curve is steep (Fig. 2a, Fig. 12). Additionally, large differences in power production can occur in specific meteorological conditions such as frontal propagation.

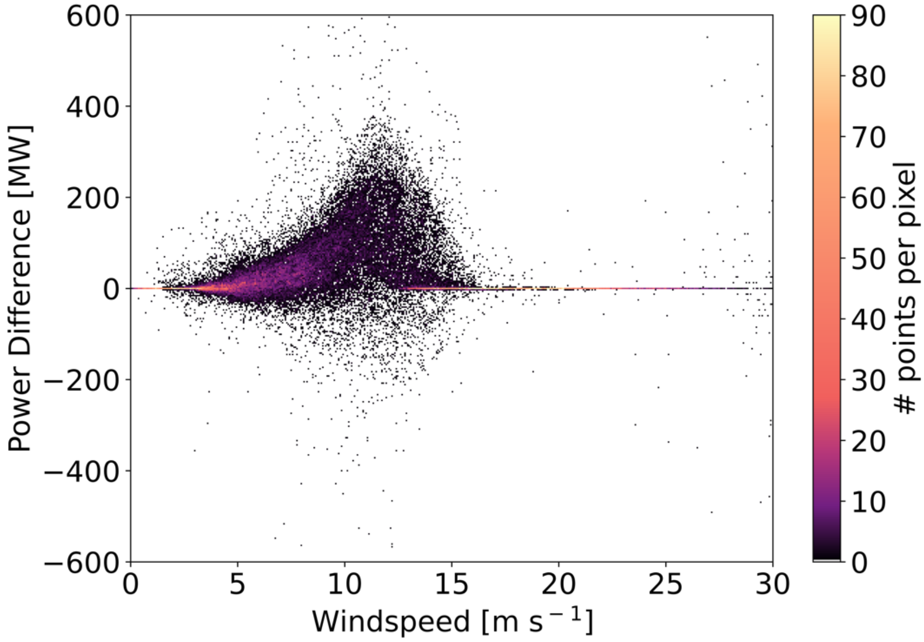

Fig. 12. The difference in power production (TKE_100-TKE_0) at Vineyard Wind as a function of wind speed. Colored contouring depicts the density of scattered points per pixel. Wind speeds are obtained every 10 m from a point centered on Vineyard Wind at the hub height.

Comparison of power production between TKE amounts by other meteorological variables lacked significant trends. For example, we additionally analyzed differences in power production by wind direction, following the hypothesis that northerly wind directions could transport more turbulence to Vineyard Wind because land has a higher roughness length than the ocean. TKE_100 runs may harness this mechanical turbulence more for wake replenishment. Analysis of differences in power production by PBL height also failed to show significant patterns. We assumed that higher PBL heights indicated a greater reservoir of turbulence from which TKE_100 runs could replenish the wake, resulting in greater power production. Further

https://doi.org/10.5194/wes-2023-38
Preprint. Discussion started: 4 May 2023

analysis concluded by comparing power differences with the aforementioned variables' rates of change. However, we reached the same conclusions, as higher densities of scattered points occurred around frequently occurring conditions such as southwesterly wind directions.

Wake strength varies spatiotemporally between TKE_0 and TKE_100 runs. While the mean difference in wind speed at hub height between TKE_100 and TKE_0 runs indicates that TKE_0 produces stronger wakes, this averaging may obscure the actual spatiotemporal variability. For example, a wind plant may have greater TKE_100 wake wind speeds while its nearby neighbor has greater TKE_0 wake wind speeds at the same point in time. Additionally, a specific wind plant may not consistently produce stronger wakes under one TKE setting. A wind plant may fluctuate between producing stronger wakes in TKE_100 runs and TKE_0 runs throughout time. This finding suggests that other boundary-layer dynamics play a role in wake strength, and the variability of power production must be explored.

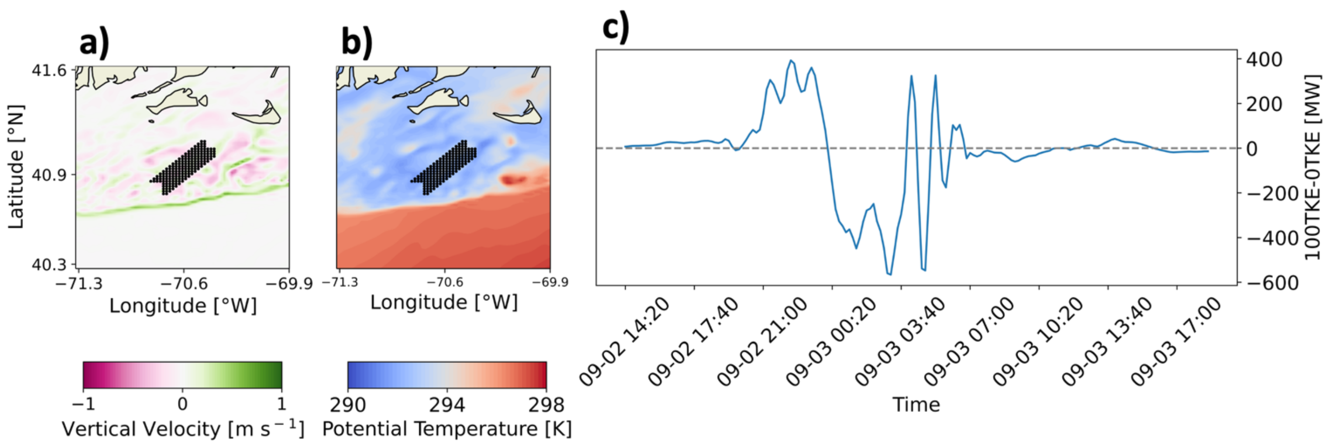

Fig. 13. Propagation of a cold front through Vineyard Wind. (a) NWF vertical wind speed is shown as the colored contour with upward vertical velocities in greens and downward vertical velocities in purples. (b) NWF potential temperature is shown with lower temperatures in blues and higher temperatures in reds. In both (a) and (b), black dots indicate turbine locations. (c) The difference in power production between TKE_100 and TKE_0 shown in megawatts, with positive values indicating that TKE_100 produces more power.

We note that wind speed and numerical noise are not the only contributors to power differences. One case study analysis shows that TKE_0 and TKE_100 separately produce more power within respective 99th percentiles over a short period of time in September (Fig. 13c). Investigation reveals that a cold front propagated through Vineyard Wind from the northwest to the southeast during this period. The cold front is identified by a lenticular band of upward vertical motion at the frontal head followed by turbulent vertical motion (Fig. 13a) in addition to advection of lower potential temperatures (Fig. 13c). As the cold front approaches, more power is produced by the TKE_100 simulation and is within the 99th percentile. When the frontal head first interacts with Vineyard Wind, more power is produced by the TKE_0 simulation and is within the 99th percentile. Conversely, TKE_100 produces more power following the frontal head. Frontal propagation can induce Kelvin–Helmholtz instabilities, the turbulence of which may aid wake recovery by vertically mixing momentum (Jiang, 2021). Increased turbulence in the TKE_100 simulation can harness more downward vertical transport of momentum from Kelvin–Helmholtz instabilities aft of the frontal head, increase wake replenishment, and produce more power.

4 Conclusions

This modeling study assesses the variability of wake effects across the mid-Atlantic OCS based on yearlong simulations, including uncertainty quantification and approaches for distinguishing internal and external wake effects. In addition to a simulation without wind plants (NWF), validated by comparison to floating lidar observations, three wind plant layouts are explored including the Vineyard Wind Lease Area alone (VW_only), all lease areas (LA), and the lease areas plus the call areas (CA). Modifying the added TKE amount (TKE_0 or TKE_100) by turbines provides uncertainty quantification in power production estimates.

The OCS is characterized by more frequent unstable stratification during winter and stable stratification during summer (Bodini et al., 2019; Optis et al., 2020; Debnath et al., 2021). In stable conditions, wakes are stronger and propagate further downwind, (Fitch et al., 2013; Vanderwende et al., 2016; Porté-Agel et al., 2020). In the worst-case scenario where downwind wake recovery diminishes during stable stratification at TKE_100, mean wakes propagate 58 km downwind. While wakes may not reach downwind clusters on average, inter-cluster waking occurs intermittently. While TKE_0 produces stronger wakes than TKE_100, downwind propagation distance differs by only 2 km.

Reduced wake wind speeds affect power production. Yearly averaged wake losses induce a 35.9% power deficit at Vineyard Wind. This deficit is composed of both internal and external waking. External wakes induce yearly averaged power losses of 14.7% (TKE_0) or 13.4% (TKE_100) while wakes from the CA induce similar losses of 14.3% over 4 months. Internal wakes at Vineyard Wind promote larger power losses of 29.2% (TKE_0) or 25.7% (TKE_100). Wake-induced power losses vary seasonally with smaller diurnal variability. Larger power deficits occur during summer, where frequent stable conditions limit wake erosion. Although upwind clusters may generate strong external wakes among the LA, wind plant orientation with respect to prevailing winds can reduce adverse impacts from nearby neighbours. Ample distance for replenishment of external wakes by the CA moderates the negative effects. Internal wake losses remain larger due to shorter distances with limited wake recovery. Both external and internal wake-induced losses grow in summer stably stratified conditions. These losses similarly increase in strength for TKE_0 simulations from inhibited recovery.

https://doi.org/10.5194/wes-2023-38
Preprint. Discussion started: 4 May 2023

eawe european academy of wind energy
Open Access WIND ENERGY SCIENCE DISCUSSIONS

Resolving precise wake losses and AEP are crucial for stakeholders and grid operators. In the absence of wakes, Vineyard Wind could supply 10.02% of New England's demand. Operating alone, Vineyard Wind's supply reduces to 7.94% (TKE_0) or 8.24% (TKE_100). Adding external wakes from the LA, Vineyard Wind's annual supply lessens to 7.07% (TKE_0) or 7.47% (TKE_100). Although wakes are stronger among the LA, the greater number of turbines can meet 58.82% (TKE_0) and 61.22% (TKE_100) of New England's demand, or roughly 1.72% and 1.65% of national demand. However, the LA only satisfy demand about 25% of the time on an hourly basis. Overall, spring features maximum power production with the fastest hub-height wind speeds. Wind speeds are slower in summer, reducing power production during July and August, which have featured New England's top-10 utility demand days since 1997 (NEISO, 2023b).

Variable TKE amounts marginally impact power generation. TKE_0 simulations average 3.8% less production than TKE_100 throughout the year, as reduced turbulence in TKE_0 limits momentum transport into the waked zone. Although differences in power production are small, both simulations exhibit large variability at short temporal periods. Improving WFP accuracy by accounting for wind shear throughout the rotor-swept region (Redfern et al., 2019) and dynamic air density may increase the variability in power production further (Wu et al., 2022).

Future wind resource assessments may neglect differences between TKE_0 and TKE_100 because the power production offset is minor, although we identify a strong outlier during a frontal passage when differences in power production between TKE_100 and TKE_0 are large. While power production differences are minor, effects on other atmospheric variables may be more significant (Fig. A1). Variability may be influenced by other meteorological conditions. Successive analyses should consider yearlong CA simulations to identify the full range of external wake impacts. Although we infer that the effects of CA wakes on Vineyard Wind are small relative to LA wakes, yearlong estimates may show otherwise. Notably, we find that internal wakes have larger impacts on power production than those generated externally.

5 Appendices

5.1 Appendix A

To assess the sensitivity of simulations to the amount of parameterized TKE, we conducted a set of 2-day test runs from 11 to 13 July 2017. This time period was chosen for its predominance of southwesterly winds, which represent typical conditions across the OCS and for the availability of Air-Sea Interaction Tower lidar observations for wind profile validation of the NWF simulations. Test runs consist of 0% (TKE_0), 25% (TKE_25), 50% (TKE_50), and 100% (TKE_100) added TKE with the WFP.

https://doi.org/10.5194/wes-2023-38
Preprint. Discussion started: 4 May 2023

eawe european academy of wind energy
Open Access WIND ENERGY SCIENCE DISCUSSIONS

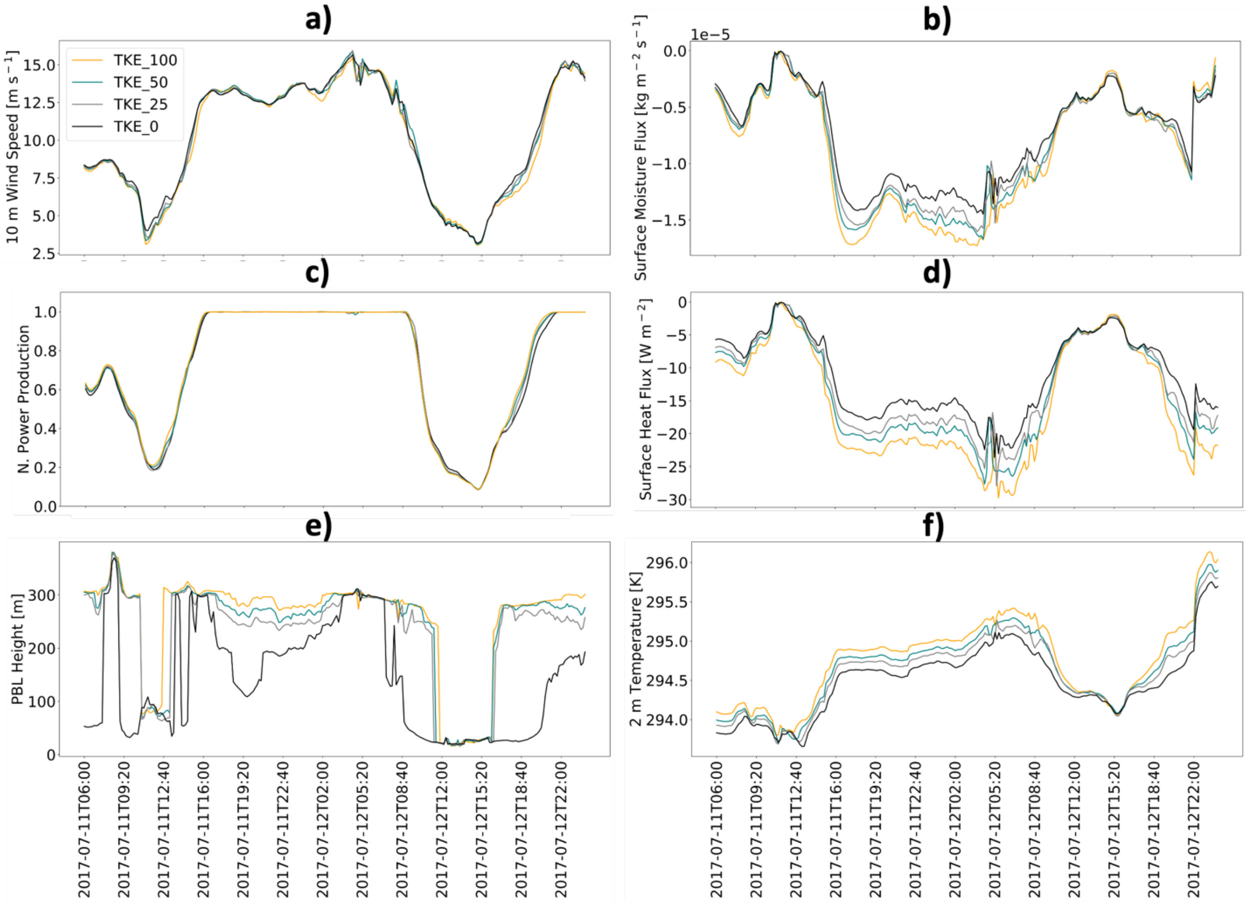

Fig. A1. The effects of modifying the amount of turbulent kinetic energy (TKE) during test runs. Panels show (a) 10-m wind speed, (b) surface moisture flux, (c) normalized power production, (d) surface heat flux, (e) planetary boundary layer (PBL) height, and (f) 2-m temperature. Values are collected from a point centered on Vineyard Wind. Power production is the sum of all cells containing turbines. TKE_100 is shown in orange, TKE_50 in blue, TKE_25 in gray, and TKE_0 in black.

Larger variations between wind speeds (Fig. A1a) correspond with larger spreads in power output by TKE amount (Fig. A1b). The differences in power production driven by TKE amount are precise. Because power production totals for TKE_25 and TKE_50 are typically bounded by the totals for TKE_0 and TKE_100, production simulations incorporate TKE_0 and TKE_100 only to account for the full range of uncertainty throughout a full yearlong period from 01 September 2019 to 01 September 2020.

Although subtle, several important meteorological quantities from the model grid cell at the center of Vineyard Wind vary by the added TKE amount. For example, wind speeds are slower around 12 July between 12:00 and 15:20 UTC (Fig. A1a). The wind speed reduction causes a corresponding decrease in turbulent transport of moisture. The mean difference in moisture

https://doi.org/10.5194/wes-2023-38
Preprint. Discussion started: 4 May 2023

fluxes throughout the period between TKE_100 and TKE_0 is 1.39×10^{-6} kg m^{-2} s^{-1} (Fig. A1b). Note that the surface moisture flux remains negative throughout the period. While maritime moisture profiles typically exhibit a decrease in concentration with height, corresponding with a positive flux, mixing from the turbines reduces the near-surface concentration and reverses the gradient.

Heat flux exhibits large variability. The mean difference in heat flux throughout the period between TKE_100 and TKE_0 is 4.15 W m^{-2} (Fig. A1d). The wind speed decrease between 12:00 and 15:20 UTC reduces surface stresses and turbulent transport of heat. The reduction in heat flux causes 2-m temperatures to decrease and exhibit less variability by TKE amount, with a mean difference of 0.26 K between TKE_100 and TKE_0 (Fig. A1f).

The reduction in turbulent mixing lowers PBL height, regardless of TKE amount, between 15 to 20 m (Fig. A1e). The near-surface PBL height suppresses the small variations in turbulent mixing across test runs and causes fluxes to equalize. PBL heights differ the most by added TKE amount and may result from changes in weighting between two separate height determination methods present in the MYNN physics driver (Fig. A1c).

5.2 Appendix B

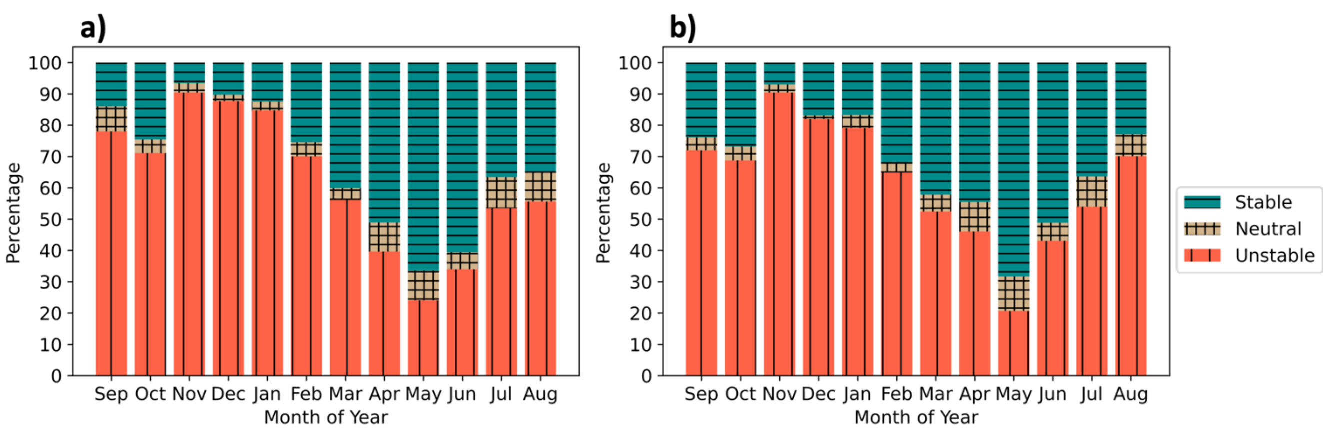

Fig. B1. Stability classification using the Obukhov length for the period 01 September 2019 to 01 September 2020 at the (a) E05 and (b) E06 lidars from NWF. Tan cross hatch are neutral stratification, blue horizontal bars are stable stratification, and red vertical bars are unstable stratification.

Stratification at the E05 and E05 lidars exhibits similar seasonal variability to Vineyard Wind (Fig. B1). The winter months feature predominant unstable stratification caused by cold air advecting over a warm sea surface. Into the spring and early

https://doi.org/10.5194/wes-2023-38
Preprint. Discussion started: 4 May 2023

summer, stratification transitions to more common stable conditions as warm air advects over a cooler sea surface. Stratification is most commonly unstable in November and stable in May.

5.3 Appendix C

Surface estimates of L may not represent stability aloft (Fig. C1) and may overestimate unstable conditions. When considering monthly averaged potential temperature profiles through the rotor layer, only November and December appear unstably stratified. While September and October appear predominantly unstable based on surface estimates, potential temperature gradients within the rotor-swept area suggest slightly stable conditions, supporting inferences that offshore conditions are stable during late summer. Therefore, our limited set of CA simulations focus on 01 September to 31 October 2019 and 01 July to 31 August 2020 for its presumed abundance of stable stratification.

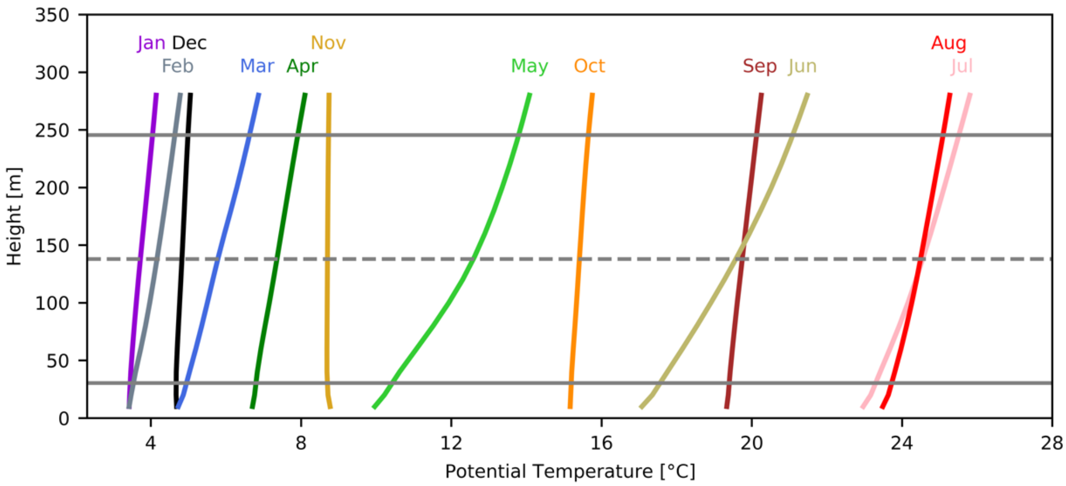

Fig. C1. Monthly averaged WRF-simulated potential temperature profiles at a point centered on Vineyard Wind. Horizontal gray lines indicate the levels of the hub height (dashed) and the rotor-swept area (solid).

5.4 Appendix D

Wakes in the simulations with CA show similar dependence on stratification (Fig. D1). Note that we simulate the CA for four months only (01 September to 31 October 2019 and 01 July to 31 August 2020) at one TKE level only (TKE_100) due to computational costs. The maximum wake strength intensifies from -1.6 m s^{-1} to -3.2 m s^{-1} moving from unstable to stable stratification (Fig. D1b,c).

https://doi.org/10.5194/wes-2023-38
Preprint. Discussion started: 4 May 2023

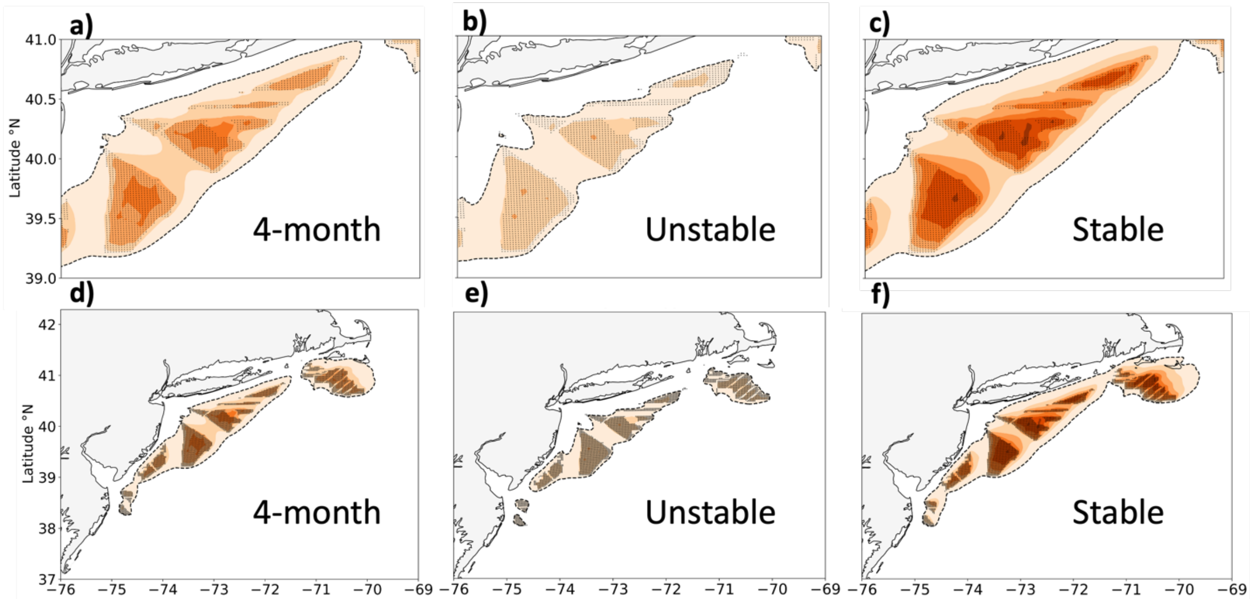

Fig. D1. Average wake wind speeds among the call areas (a,d) for the combined 4-month period, 01 September to 31 October 2019 and 01 July to 31 August 2020, (b,e) during unstable stratification, and (c,f) during stable stratification. All panels show 100% added TKE. Wake wind speed deficits are shown by the colored contour and turbines are shown as black dots.

Wake propagation distance for the call area simulation is also affected by stratification. During the 4 months considered, unstable, stable, and neutral conditions occur 48.82%, 48.74%, and 2.43% of the time, respectively. As such, there is essentially an even split between the percentage of occurrence of unstable and stable conditions. In unstable conditions, wakes from the two southernmost lease areas fail to reach neighboring downwind clusters on average, and no wakes stronger than this threshold reach the Rhode Island/Massachusetts (RIMA) block (Fig. D1e). In stable stratification, wakes from each cluster reach downwind clusters, including the RIMA block (Fig. D1f). Averaged over all 4 months, wakes between lease areas (LA) and the CA along the New Jersey and New York Bight affect each other, but no wakes reach the RIMA block. Wakes may still interact with downwind plants at individual times and affect power production.

5.5 Appendix E

Results can show evidence of numerical noise, which emerges when simulations incorporate the WFP (Ancell et al., 2018; Lauridsen and Ancell, 2018). In our simulations, these brief periods of numerical noise emerge and decay, often coincident with precipitation. While we expect differences in wake wind speed immediately downwind of power plants, it is unlikely that these differences could advect to the southeast corner of the domain, roughly 600 km southeast of Vineyard Wind (Fig. E1a). If this numerical noise occurred in grid cells with turbines, then this noise would introduce error in power estimations.

https://doi.org/10.5194/wes-2023-38
Preprint. Discussion started: 4 May 2023

We explored several approaches to mitigate the numerical noise, none of which succeeded. First, we increased the floating-point accuracy of numerical calculations by enabling double precision in WRF. Double precision limits the growth of rounding error to smaller magnitudes (Ancell et al., 2018). This attempt aimed to confine perturbations to smaller orders of magnitude that take longer amounts of time to become substantial. To prevent "runaway" error growth after long periods of time, we submit simulation restarts each month.

In observing a spatial correlation of numerical noise with convective precipitation during test runs, we reran test simulations with a more complex microphysics scheme. The Thompson microphysics scheme, used throughout, is double-moment with respect to cloud ice only. We substituted the Morrison microphysics scheme, which is fully double-moment with respect to cloud droplets and rain, cloud ice, snow, and graupel (Morrison et al., 2009). The use of Morrison microphysics did not improve numerical noise, so its computational cost could not be justified.

Next, we introduced a filter for shortwave numerical noise by prohibiting upgradient diffusion. Doing so requires setting the parameter diff_6th_opt to 2 in the namelist, as certain combinations of advection and diffusion orders are conducive to mitigating noise around heavy precipitation (Kusaka et al., 2005). While Kusaka et al. (2005) found the combination of fifth-order advection and sixth-order diffusion to perform best, we had previously attempted this combination because default advection in WRF is fifth-order. Thus, we attempted the next best recommendation—the combination of sixth-order advection and diffusion. Again, this combination did not improve results.

We made a final attempt at noise reduction by running an ensemble of three members using a stochastic kinetic energy backscatter scheme (SKEBS). Ensemble members contain seeds with variable time steps that randomly inject kinetic energy into grid cells (Berner, 2013). These stochastic supplements replenish the kinetic energy sink from unresolvable subgrid-scale processes. We followed recommendations to perturb streamfunction and potential temperature backscatter rates by 1×10^{-5} and 1×10^{-6}, respectively. Again, while subtle differences emerged between the simulations, little improvement was found.

https://doi.org/10.5194/wes-2023-38
Preprint. Discussion started: 4 May 2023

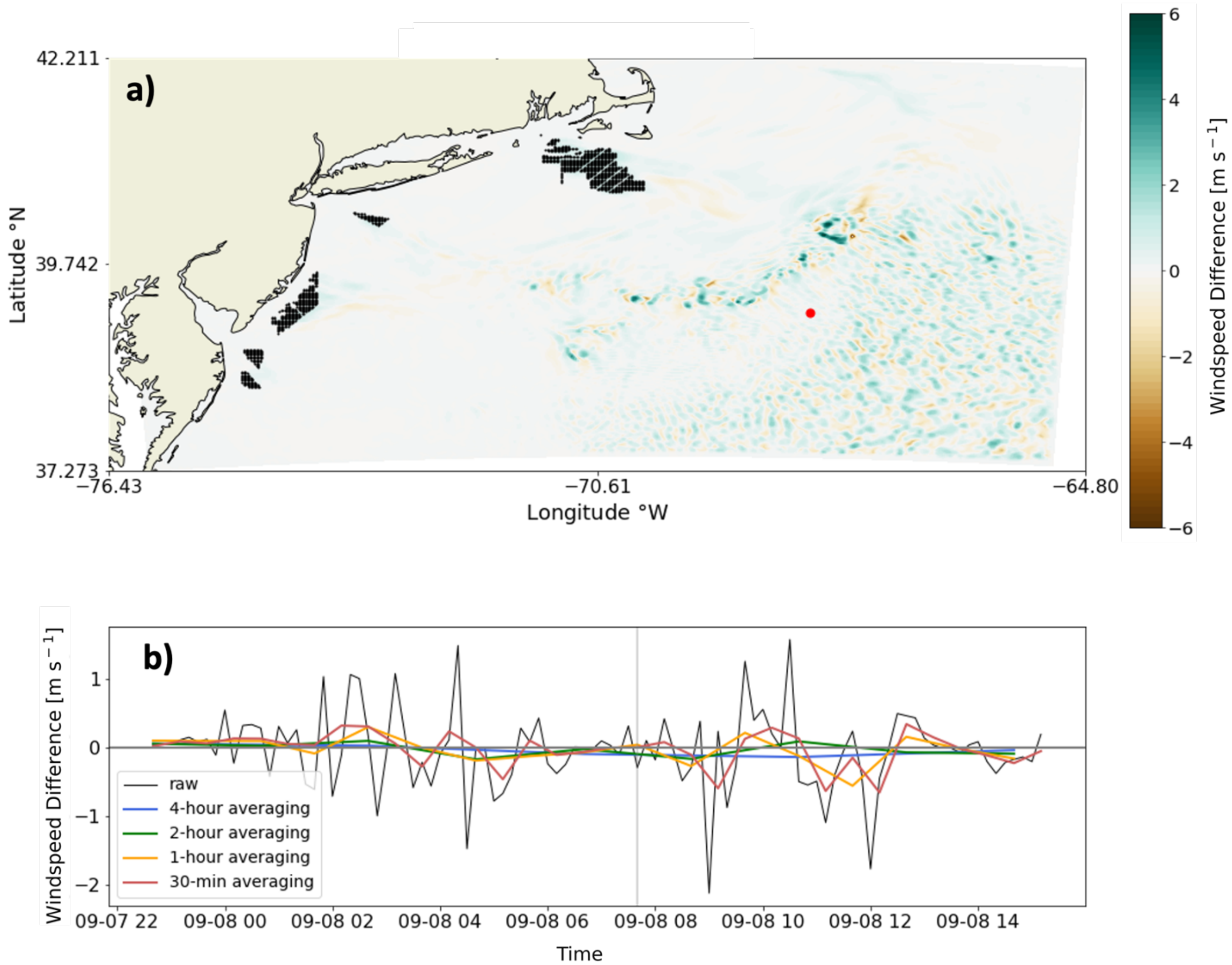

Fig. E1. (a) The wind speed difference between TKE_100 and TKE_0 at the hub height from LA runs. Turbines are shown as black dots. Blue contouring indicates TKE_100 produced faster wind speeds and vice versa. (b) Wind speeds obtained at the red circle in (a) are shown as a time series. The raw difference in wind speeds and averaging periods are shown as different line colors in the time series. The gray vertical line shows the time stamp at which the map occurs.

We saw little improvement from the aforementioned preprocessing efforts. Given this lack of improvement and a need to conserve computational resources, we employ averaging during postprocessing to alleviate the effects of noise. Modifying averaging periods impacts the range of numerical noise in the wind speed field (Fig. E1b). Although noise occurring in grid cells containing turbines poses a threat to power estimations, we show noise occurring in the southeastern portion of the domain. This underscores the point that subtraction of wind speeds between simulations with variable TKE amounts should only show differences within the wake, and such differences are a result of noise. Averaging periods provides greater relief. While 2- and 4-hour averaging periods deliver the best results, these temporal scales can hide important diurnal variability. Conversely, a 30-minute averaging period can improve results, but local extrema occasionally reach magnitudes similar to the

https://doi.org/10.5194/wes-2023-38
Preprint. Discussion started: 4 May 2023

magnitudes of the raw noise. Thus, hourly averaging can mitigate noise without masking important variability. As a final note, other researchers have found benefit by employing grid nudging within this domain above the PBL (Golbazi, M., personal communication, September 2022).

6 Code and Data Availability

The data and files that support this work are publicly available. The ERA5 boundary conditions can be downloaded from the ECMWF Climate Data Store at https://cds.climate.copernicus.eu/cdsapp#!/dataset/reanalysis-era5-pressure-levels?tab=form. Shapefiles including the bounding extents of the lease and call areas are at https://www.boem.gov/renewable-energy/mapping-and-data/renewable-energy-gis-data. Individual turbine coordinates and their power and thrust curves are provided at https://zenodo.org/record/7374283#.Y4YZxC-B1KM. WRF namelists for NWF and WFP simulations may obtained at https://zenodo.org/record/7374239#.Y4YaOy-B1KM. The simulation output data may be acquired in HDF5 format at OpenEI_link.

7 Author Contributions

Conceptualization: JKL and MO. Methodology: DR, JKL, and MO. Software: DR, AR, MR. Validation: DR. Formal analysis: DR. Investigation: DR and J.K.L. Resources: MO, NB. Writing – original draft: DR and JKL. Writing – review and editing: all co-authors. Visualization: DR. Supervision: JKL, MO, NB. Project administration: MO and NB. Funding acquisition: MO and NB.

8 Competing Interests

Author Mike Optis co-authored the submitted manuscript while an employee of the National Renewable Energy Laboratory. He has since founded Veer Renewables, which recently released a wind modeling product, WakeMap, which is based on a similar numerical weather prediction modeling framework as the one described in this manuscript. Data from WakeMap is sold to wind energy stakeholders for profit. Public content on WakeMap include a website (https://veer.eco/wakemap/), a white paper (https://veer.eco/wp-content/uploads/2023/02/WakeMap_White_Paper_Veer_Renewables.pdf) and several LinkedIn posts promoting WakeMap.

9 Acknowledgements and Statements

This work was supported by an agreement with NREL under APUP UGA-0-41026-125. This work was authored [in part] by the National Renewable Energy Laboratory, operated by Alliance for Sustainable Energy, LLC, for the U.S. Department of Energy (DOE) under Contract No. DE-AC36-08GO28308. Funding was provided by the U.S. Department of Energy Office of Energy Efficiency and Renewable Energy Wind Energy Technologies Office and by the National Offshore Wind Research and Development Consortium under agreement no. CRD-19-16351. The views expressed in the article do not necessarily represent the views of the DOE or the U.S. Government. The U.S. Government and the publisher, by accepting the article for publication, acknowledge that the U.S. Government retains a nonexclusive, paid-up, irrevocable, worldwide license to publish or reproduce the published form of this work, or allow others to do so, for U.S. Government purposes. Neither NYSERDA nor OceanTech Services/DNV have reviewed the information contained herein and the opinions in this report do not necessarily reflect those of any of these parties. A portion of computation used the Blanca condo computing resource at the University of Colorado Boulder. Blanca is jointly funded by computing users and the University of Colorado Boulder. A portion of computation used the Summit supercomputer, which is supported by the National Science Foundation (awards ACI-1532235 and ACI-1532236), the University of Colorado Boulder, and Colorado State University. The Summit supercomputer is a joint effort of the University of Colorado Boulder and Colorado State University. A portion of this research was performed using computational resources sponsored by the U.S. Department of Energy's Office of Energy Efficiency and Renewable Energy and located at the National Renewable Energy Laboratory.

10 References

218th Legislature: NJ Renewable Portfolio Standards, https://www.njleg.state.nj.us/2018/Bills/A4000/3723_I1.PDF, 2018.

Aitken, M. L., Kosović, B., Mirocha, J. D., and Lundquist, J. K.: Large eddy simulation of wind turbine wake dynamics in the stable boundary layer using the Weather Research and Forecasting Model, Journal of Renewable and Sustainable Energy, 6, 033137, https://doi.org/10.1063/1.4885111, 2014.

Ancell, B. C., Bogusz, A., Lauridsen, M. J., and Nauert, C. J.: Seeding Chaos: The Dire Consequences of Numerical Noise in NWP Perturbation Experiments, Bull. Amer. Meteor. Soc., 99, 615–628, https://doi.org/10.1175/BAMS-D-17-0129.1, 2018.

Antonini, E. G. A., Romero, D. A., and Amon, C. H.: Optimal design of wind farms in complex terrains using computational fluid dynamics and adjoint methods, Applied Energy, 261, 114426, https://doi.org/10.1016/j.apenergy.2019.114426, 2020.

https://doi.org/10.5194/wes-2023-38
Preprint. Discussion started: 4 May 2023

Archer, C. L., Colle, B. A., Veron, D. L., Veron, F., and Sienkiewicz, M. J.: On the predominance of unstable atmospheric conditions in the marine boundary layer offshore of the U.S. northeastern coast, Journal of Geophysical Research: Atmospheres, 121, 8869–8885, https://doi.org/10.1002/2016JD024896, 2016.

Archer, C. L., Wu, S., Ma, Y., and Jiménez, P. A.: Two Corrections for Turbulent Kinetic Energy Generated by Wind Farms in the WRF Model, Monthly Weather Review, 148, 4823–4835, https://doi.org/10.1175/MWR-D-20-0097.1, 2020.

Arthur, R. S., Mirocha, J. D., Marjanovic, N., Hirth, B. D., Schroeder, J. L., Wharton, S., and Chow, F. K.: Multi-Scale Simulation of Wind Farm Performance during a Frontal Passage, Atmosphere, 11, 245, https://doi.org/10.3390/atmos11030245, 2020.

Beiter, P., Musial, W., Duffy, P., Cooperman, A., Shields, M., Heimiller, D., and Optis, M.: The Cost of Floating Offshore Wind Energy in California Between 2019 and 2032, Renewable Energy, 113, 2020.

Berner, J.: WRF Implementation Details and Version history of a Stochastic Kinetic-Energy Backscatter Scheme (SKEBS), National Center for Atmospheric Research Tech. Note, 21, 2013.

Bodini, N., Lundquist, J. K., and Kirincich, A.: U.S. East Coast Lidar Measurements Show Offshore Wind Turbines Will Encounter Very Low Atmospheric Turbulence, Geophysical Research Letters, 46, 5582–5591, https://doi.org/10.1029/2019GL082636, 2019.

BOEM: Renewable Energy GIS Data | Bureau of Ocean Energy Management, https://www.boem.gov/renewable-energy/mapping-and-data/renewable-energy-gis-data, n.d.

Burton, T., Jenkins, N., Sharpe, D., and Bossanyi, E.: Wind Energy Handbook, John Wiley & Sons, 784 pp., 2011.

Debnath, M., Doubrawa, P., Optis, M., Hawbecker, P., and Bodini, N.: Extreme wind shear events in US offshore wind energy areas and the role of induced stratification, Wind Energy Science, 6, 1043–1059, https://doi.org/10.5194/wes-6-1043-2021, 2021.

DNV: NYSERDA Floating LiDAR Buoy Data, https://oswbuoysny.resourcepanorama.dnvgl.com/download/f67d14ad-07ab-4652-16d2-08d71f257da1, 2022.

NYSERDA Floating LiDAR Buoy Data: https://oswbuoysny.resourcepanorama.dnv.com/, last access: 18 March 2023.

Donlon, C. J., Martin, M., Stark, J., Roberts-Jones, J., Fiedler, E., and Wimmer, W.: The Operational Sea Surface Temperature and Sea Ice Analysis (OSTIA) system, Remote Sensing of Environment, 116, 140–158, https://doi.org/10.1016/j.rse.2010.10.017, 2012.

EIA: Frequently Asked Questions (FAQs) - U.S. Energy Information Administration (EIA), https://www.eia.gov/tools/faqs/faq.php, 2023.

Fischereit, J., Brown, R., Larsén, X. G., Badger, J., and Hawkes, G.: Review of Mesoscale Wind-Farm Parametrizations and Their Applications, Boundary-Layer Meteorol, 182, 175–224, https://doi.org/10.1007/s10546-021-00652-y, 2022.

Fitch, A. C., Olson, J. B., Lundquist, J. K., Dudhia, J., Gupta, A. K., Michalakes, J., and Barstad, I.: Local and Mesoscale Impacts of Wind Farms as Parameterized in a Mesoscale NWP Model, Monthly Weather Review, 140, 3017–3038, https://doi.org/10.1175/MWR-D-11-00352.1, 2012.

Fitch, A. C., Lundquist, J. K., and Olson, J. B.: Mesoscale Influences of Wind Farms throughout a Diurnal Cycle, Mon. Wea. Rev., 141, 2173–2198, https://doi.org/10.1175/MWR-D-12-00185.1, 2013.

Golbazi, M., Archer, C. L., and Alessandrini, S.: Surface impacts of large offshore wind farms, Environ. Res. Lett., 17, 064021, https://doi.org/10.1088/1748-9326/ac6e49, 2022.

Gupta, T. and Baidya Roy, S.: Recovery Processes in a Large Offshore Wind Farm, Wind Energy Science Discussions, 1–23, https://doi.org/10.5194/wes-2021-7, 2021.

Hahmann, A. N., Sīle, T., Witha, B., Davis, N. N., Dörenkämper, M., Ezber, Y., García-Bustamante, E., González-Rouco, J. F., Navarro, J., Olsen, B. T., and Söderberg, S.: The making of the New European Wind Atlas – Part 1: Model sensitivity, Geoscientific Model Development, 13, 5053–5078, https://doi.org/10.5194/gmd-13-5053-2020, 2020.

Hersbach, H., Bell, B., Berrisford, P., Hirahara, S., Horányi, A., Muñoz-Sabater, J., Nicolas, J., Peubey, C., Radu, R., Schepers, D., Simmons, A., Soci, C., Abdalla, S., Abellan, X., Balsamo, G., Bechtold, P., Biavati, G., Bidlot, J., Bonavita, M., De Chiara, G., Dahlgren, P., Dee, D., Diamantakis, M., Dragani, R., Flemming, J., Forbes, R., Fuentes, M., Geer, A., Haimberger, L., Healy, S., Hogan, R. J., Hólm, E., Janisková, M., Keeley, S., Laloyaux, P., Lopez, P., Lupu, C., Radnoti, G., de Rosnay, P., Rozum, I., Vamborg, F., Villaume, S., and Thépaut, J.-N.: The ERA5 global reanalysis, Quarterly Journal of the Royal Meteorological Society, 146, 1999–2049, https://doi.org/10.1002/qj.3803, 2020.

Iacono, M. J., Delamere, J. S., Mlawer, E. J., Shephard, M. W., Clough, S. A., and Collins, W. D.: Radiative forcing by long-lived greenhouse gases: Calculations with the AER radiative transfer models, Journal of Geophysical Research: Atmospheres, 113, https://doi.org/10.1029/2008JD009944, 2008.

Jiang, Q.: Impact of Elevated Kevin-Helmholtz Billows on the Atmospheric Boundary Layer, Journal of the Atmospheric Sciences, 1, https://doi.org/10.1175/JAS-D-21-0062.1, 2021.

Kain, J. S.: The Kain–Fritsch Convective Parameterization: An Update, Journal of Applied Meteorology and Climatology, 43, 170–181, https://doi.org/10.1175/1520-0450(2004)043<0170:TKCPAU>2.0.CO;2, 2004.

https://doi.org/10.5194/wes-2023-38
Preprint. Discussion started: 4 May 2023

Kusaka, H., Crook, A., Knievel, J. C., and Dudhia, J.: Sensitivity of the WRF Model to Advection and Diffusion Schemes for Simulation of Heavy Rainfall along the Baiu Front, SOLA, 1, 177–180, https://doi.org/10.2151/sola.2005-046, 2005.

Lauridsen, M. J. and Ancell, B. C.: Nonlocal Inadvertent Weather Modification Associated with Wind Farms in the Central United States, Advances in Meteorology, 2018, e2469683, https://doi.org/10.1155/2018/2469683, 2018.

Lee, J. C. Y. and Fields, M. J.: An overview of wind-energy-production prediction bias, losses, and uncertainties, Wind Energy Science, 6, 311–365, https://doi.org/10.5194/wes-6-311-2021, 2021.

Livingston, H. G. and Lundquist, J. K.: How many offshore wind turbines does New England need?, Meteorological Applications, 27, e1969, https://doi.org/10.1002/met.1969, 2020.

Lundquist, J. K., DuVivier, K. K., Kaffine, D., and Tomaszewski, J. M.: Costs and consequences of wind turbine wake effects arising from uncoordinated wind energy development, Nature Energy, 4, 26–34, https://doi.org/10.1038/s41560-018-0281-2, 2019.

Mirocha, J. D., Kosovic, B., Aitken, M. L., and Lundquist, J. K.: Implementation of a generalized actuator disk wind turbine model into the weather research and forecasting model for large-eddy simulation applications, Journal of Renewable and Sustainable Energy, 6, 013104, https://doi.org/10.1063/1.4861061, 2014.

Monin, A. S. and Obukhov, A. M.: Basic laws of turbulent mixing in the surface layer of the atmosphere, Tr. Akad. Nauk SSSR Geophiz. Inst., 24, 30, 1954.

Morrison, H., Thompson, G., and Tatarskii, V.: Impact of Cloud Microphysics on the Development of Trailing Stratiform Precipitation in a Simulated Squall Line: Comparison of One- and Two-Moment Schemes, Monthly Weather Review, 137, 991–1007, https://doi.org/10.1175/2008MWR2556.1, 2009.

Musial, W., Heimiller, D., Beiter, P., Scott, G., and Draxl, C.: 2016 Offshore Wind Energy Resource Assessment for the United States, https://doi.org/10.2172/1324533, 2016.

Nakanishi, M. and Niino, H.: An Improved Mellor–Yamada Level-3 Model: Its Numerical Stability and Application to a Regional Prediction of Advection Fog, Boundary-Layer Meteorol, 119, 397–407, https://doi.org/10.1007/s10546-005-9030-8, 2006.

NEISO: ISO New England - Energy, Load, and Demand Reports, https://www.iso-ne.com/isoexpress/web/reports/load-and-demand/-/tree/dmnd-rt-hourly-sys, 2023a.

NEISO: Reliable Electricity. Competitive Prices. Clean-Energy Transition., https://www.iso-ne.com, 2023b.

Niu, G.-Y., Yang, Z.-L., Mitchell, K. E., Chen, F., Ek, M. B., Barlage, M., Kumar, A., Manning, K., Niyogi, D., Rosero, E., Tewari, M., and Xia, Y.: The community Noah land surface model with multiparameterization options (Noah-MP): 1. Model description and evaluation with local-scale measurements, Journal of Geophysical Research: Atmospheres, 116, https://doi.org/10.1029/2010JD015139, 2011.

Nygaard, N. G.: Wakes in very large wind farms and the effect of neighbouring wind farms, J. Phys.: Conf. Ser., 524, 012162, https://doi.org/10.1088/1742-6596/524/1/012162, 2014.

Optis, M., Bodini, N., Debnath, M., and Doubrawa, P.: Best Practices for the Validation of U.S. Offshore Wind Resource Models, National Renewable Energy Lab. (NREL), Golden, CO (United States), https://doi.org/10.2172/1755697, 2020.

Platis, A., Siedersleben, S. K., Bange, J., Lampert, A., Bärfuss, K., Hankers, R., Cañadillas, B., Foreman, R., Schulz-Stellenfleth, J., Djath, B., Neumann, T., and Emeis, S.: First in situ evidence of wakes in the far field behind offshore wind farms, Sci Rep, 8, 2163, https://doi.org/10.1038/s41598-018-20389-y, 2018.

Porté-Agel, F., Bastankhah, M., and Shamsoddin, S.: Wind-Turbine and Wind-Farm Flows: A Review, Boundary-Layer Meteorol, 174, 1–59, https://doi.org/10.1007/s10546-019-00473-0, 2020.

Pronk, V., Bodini, N., Optis, M., Lundquist, J. K., Moriarty, P., Draxl, C., Purkayastha, A., and Young, E.: Can reanalysis products outperform mesoscale numerical weather prediction models in modeling the wind resource in simple terrain?, Wind Energ. Sci., 7, 487–504, https://doi.org/10.5194/wes-7-487-2022, 2022.

Pryor, S. C., Barthelmie, R. J., and Shepherd, T. J.: Wind power production from very large offshore wind farms, Joule, 5, 2663–2686, https://doi.org/10.1016/j.joule.2021.09.002, 2021.

Redfern, S., Olson, J. B., Lundquist, J. K., and Clack, C. T. M.: Incorporation of the Rotor-Equivalent Wind Speed into the Weather Research and Forecasting Model's Wind Farm Parameterization, Mon. Wea. Rev., 147, 1029–1046, https://doi.org/10.1175/MWR-D-18-0194.1, 2019.

Rybchuk, A., Juliano, T. W., Lundquist, J. K., Rosencrans, D., Bodini, N., and Optis, M.: The sensitivity of the fitch wind farm parameterization to a three-dimensional planetary boundary layer scheme, Wind Energy Science, 7, 2085–2098, https://doi.org/10.5194/wes-7-2085-2022, 2022.

Schneemann, J., Rott, A., Dörenkämper, M., Steinfeld, G., and Kühn, M.: Cluster wakes impact on a far-distant offshore wind farm's power, Wind Energy Science, 5, 29–49, https://doi.org/10.5194/wes-5-29-2020, 2020.

Shapiro, C. R., Gayme, D. F., and Meneveau, C.: Filtered actuator disks: Theory and application to wind turbine models in large eddy simulation, Wind Energy, 22, 1414–1420, https://doi.org/10.1002/we.2376, 2019.

Siedersleben, S. K., Platis, A., Lundquist, J. K., Djath, B., Lampert, A., Bärfuss, K., Cañadillas, B., Schulz-Stellenfleth, J., Bange, J., Neumann, T., and Emeis, S.: Turbulent kinetic energy over large offshore wind farms observed and simulated by the mesoscale model WRF (3.8.1), Geoscientific Model Development, 13, 249–268, https://doi.org/10.5194/gmd-13-249-2020, 2020.

Skamarock, W. C., Klemp, J. B., Dudhia, J., Gill, D. O., Liu, Z., Berner, J., Wang, W., Powers, J. G., Duda, M. G., and Barker, D. M.: A description of the advanced research WRF model version 4, 2019.

Stevens, R. J. A. M., Gayme, D. F., and Meneveau, C.: Effects of turbine spacing on the power output of extended wind-farms, Wind Energy, 19, 359–370, https://doi.org/10.1002/we.1835, 2016.

Stoelinga, M., Sanchez-Gomez, M., Poulos, G. S., and Crescenti, J.: Estimating Long-Range External Wake Losses in Energy Yield and Operational Performance Assessments Using the WRF Wind Farm Parameterization, 2022.

Thompson, G., Field, P. R., Rasmussen, R. M., and Hall, W. D.: Explicit Forecasts of Winter Precipitation Using an Improved Bulk Microphysics Scheme. Part II: Implementation of a New Snow Parameterization, Monthly Weather Review, 136, 5095–5115, https://doi.org/10.1175/2008MWR2387.1, 2008.

Tomaszewski, J. M. and Lundquist, J. K.: Simulated wind farm wake sensitivity to configuration choices in the Weather Research and Forecasting model version 3.8.1, Geoscientific Model Development, 13, 2645–2662, https://doi.org/10.5194/gmd-13-2645-2020, 2020.

Vanderwende, B. J., Kosović, B., Lundquist, J. K., and Mirocha, J. D.: Simulating effects of a wind-turbine array using LES and RANS, Journal of Advances in Modeling Earth Systems, 8, 1376–1390, https://doi.org/10.1002/2016MS000652, 2016.

Virtanen, P., Gommers, R., Oliphant, T. E., Haberland, M., Reddy, T., Cournapeau, D., Burovski, E., Peterson, P., Weckesser, W., Bright, J., van der Walt, S. J., Brett, M., Wilson, J., Millman, K. J., Mayorov, N., Nelson, A. R. J., Jones, E., Kern, R., Larson, E., Carey, C. J., Polat, İ., Feng, Y., Moore, E. W., VanderPlas, J., Laxalde, D., Perktold, J., Cimrman, R., Henriksen, I., Quintero, E. A., Harris, C. R., Archibald, A. M., Ribeiro, A. H., Pedregosa, F., and van Mulbregt, P.: SciPy 1.0: fundamental algorithms for scientific computing in Python, Nat Methods, 17, 261–272, https://doi.org/10.1038/s41592-019-0686-2, 2020.

Volker, P. J. H., Badger, J., Hahmann, A. N., and Ott, S.: The Explicit Wake Parametrisation V1.0: a wind farm parametrisation in the mesoscale model WRF, Geosci. Model Dev., 8, 3715–3731, https://doi.org/10.5194/gmd-8-3715-2015, 2015.

https://doi.org/10.5194/wes-2023-38
Preprint. Discussion started: 4 May 2023

W.F. Baird & Associates: Vessel Navigation Through the Proposed Rhode Island/Massachusetts and Massachusetts Wind Energy Areas, https://static1.squarespace.com/static/5a2eae32be42d64ed467f9d1/t/5dd3d3e476d4226b2a83db25/1574163438896/Proposed+1x1+layout+from+RI-MA+Leaseholders+1+Nov+19+%281%29.pdf, 31 October 2019.

White House, T.: FACT SHEET: Biden Administration Jumpstarts Offshore Wind Energy Projects to Create Jobs, https://www.whitehouse.gov/briefing-room/statements-releases/2021/03/29/fact-sheet-biden-administration-jumpstarts-offshore-wind-energy-projects-to-create-jobs/, 29 March 2021.

Wu, C., Luo, K., Wang, Q., and Fan, J.: A refined wind farm parameterization for the weather research and forecasting model, Applied Energy, 306, 118082, https://doi.org/10.1016/j.apenergy.2021.118082, 2022.

Xia, G., Draxl, C., Optis, M., and Redfern, S.: Detecting and characterizing simulated sea breezes over the US northeastern coast with implications for offshore wind energy, Wind Energy Science, 7, 815–829, https://doi.org/10.5194/wes-7-815-2022, 2022.